Charge transfer from $CuInS_2$ quantum dots for solar cells

Jianhui SUN
Doctoral Program in Frontier Science

Submitted to the Graduate School of
Pure and Applied Sciences
in Partial Fulfillment of the Requirements
for the Degree of Doctor of Philosophy in
Science

at the
University of Tsukuba

Abstract

The ultrafast carrier dynamics in $CuInS_2$ quantum dots (QDs) was studied by means of femtosecond transient absorption spectroscopy. The size-dependent 1S transition energy determined from bleaching spectra is in agreement with that calculated on the finite-depth-well model in the effective mass approximation. The transient absorption bleaching comes from filling of electron quantized levels, allowing us to know the dynamics of the 1S electron in $CuInS_2$ QDs. The sub-100-ps electron trapping at surface defects in bare QDs accelerates with decreasing the QD size, while is effectively suppressed in well-passivated $CuInS_2$/ZnS core/shell QDs.

The electron transfer from $CuInS_2$/ZnS core/shell QDs into porous anatase TiO_2 films was studied by time-resolved photoluminescence spectroscopy. The rate and efficiency of electron transfer can be controlled by changing the core diameter and the shell thickness. The electron transfer rate reaches $10^7 s^{-1}$ for different-sized $CuInS_2$ core QDs. It is found that the electron transfer rates decrease exponentially at the decay constants of 1.1 and 1.4 nm^{-1} with increasing ZnS shell thickness for core diameters of 2.5 and 4.0 nm, respectively, in agreement with the electron tunneling model. This shows that optimized electron transfer efficiency can be realized by controlling the core/shell structures in QDs.

The QDs-sensitized solar cells (QDSSCs) consisting of a TiO_2 films co-sensitized with $CuInS_2$/CdS core/shell QDs and CdS buffer layers was fabricated. The performance of the QDSSCs assembled with $CuInS_2$/CdS core/shell QDs were superior to those assembled with $CuInS_2$/ZnS core/shell QDs. The improved performance of QDSSCs with

CuInS$_2$/CdS core/shell QDs was attributed to high efficiency of the electron transfer into TiO$_2$ films. The high efficiency came from the enhanced delocalization of electron wave function from core to CdS shell due to lower conduction band offset. Furthermore, the TiO$_2$ films were coated with the in situ growth of CdS layers by means of successive ionic layer adsorption and reaction. The CdS layers provides high surface coverage to prevent interfacial recombination between TiO$_2$ films and electrolyte. Under AM 1.5G illumination at 100 mW cm^{-2}, the CdS-CuInS$_2$ /CdS core/shell QDs co-sensitized solar cells exhibited a short-circuit photocurrent (J_{SC}) of 9.3 mA cm^{-2} , an open-circuit photovoltage (V_{OC}) of 0.48 V, a fill factor of 0.50 and a power conversion efficiency of 2.27%. The photocurrent resulting from the CuInS$_2$ QDs is increased because of the CdS coating. The CdS coating facilitated the separation of photogenerated electrons and holes in the CuInS$_2$ QDs to the electrode.

Contents

Chapter 1

General introduction

Sunlight is an abundant and renewable energy resource, and converting sunlight into electricity has been considered as one of the most promising pathway to provide clean energy. Dye sensitized solar cells (DSSCs) become a promising candidate for offering low cost solar energy, since they can be fabricated by solution-based processing, such as dip coating, screen printing, painting and roll-to-roll processing. However, DSSCs are much less stable so that the devices last less time because of the photo-degradation of the dyes.

Instead of molecular dyes, inorganic quantum dots (QDs) are considered as highly promising in next-generation solar cells, because QDs have the following advantages:[1–7] (1) easy tuning of the optical band gap energy by controlling the QD size and composition; (2) large extinction coefficient, enabling the thickness of the device to be thinner; (3) higher stability than dyes toward water and oxygen; (4) capacity for generating multiple excitons from single-photon absorption, through the impact ionization effect, which could boost the theoretical power conversion efficiency beyond the Shockley-Queisser limit of 33%.[8]

The chalcopyrite-type I-III-VI$_2$ QDs have been proposed because of their less-toxic components. Among them, CuInS$_2$ QDs are important candidates for optoelectronic devices, because bulk CuInS$_2$ has a direct band gap of 1.53 eV, which is well matched
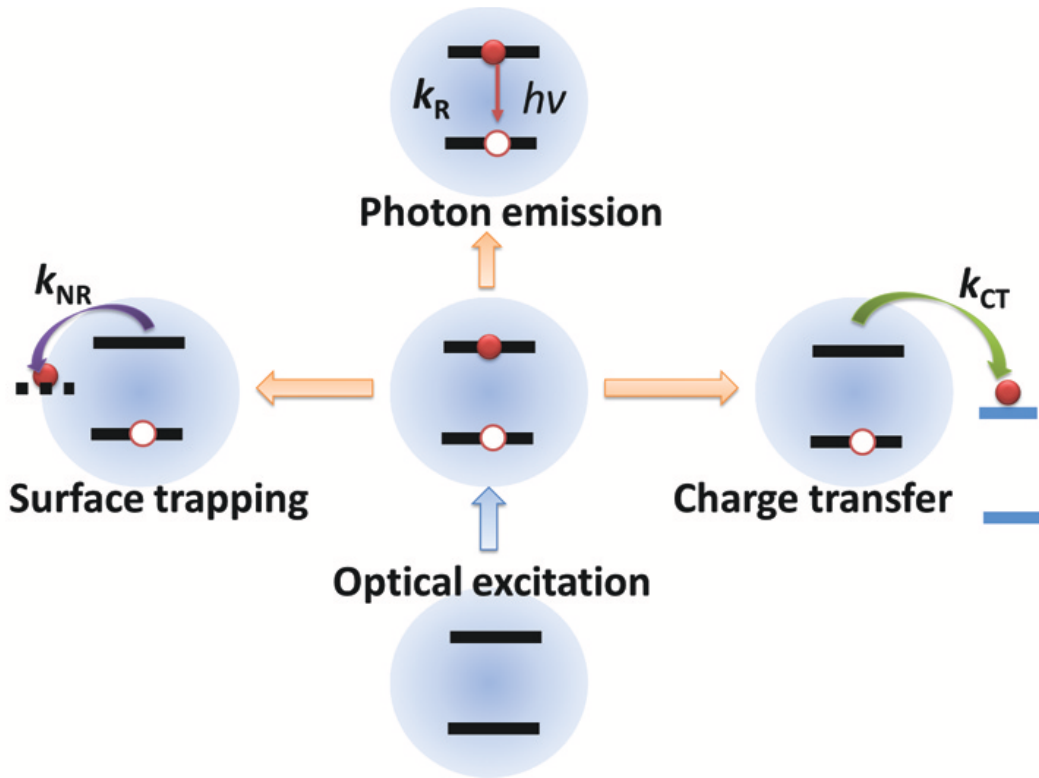
FIG. 1.1 Schematic depiction of electron hole pair generation, trapping at surface, conversion to emitted photons and charge transfer to external electrodes. The competition among them determines the charge separation efficiencies from CuInS$_2$ QDs.

with the optimal spectral range for photovoltaic applications. Furthermore, the band gap of CuInS$_2$ QDs can be tuned not only by controlling their size[9, 10] and stoichiometry[11, 12] but also by introducing other elements such as Zn.[13–15] Therefore, they are considered to be alternative low-toxicity materials as solar harvesters for QDs sensitized solar cells (QDSSCs).

In QDSSCs, efficient charge transfer from QDs to external electrodes is a key factor to achieve high power conversion efficiency. The overall charge separation efficiency from CuInS$_2$ sensitizers, as illustrated in Fig. 1.1, depends on the competitions among photon emission, charge trapping at surface defects and charge transfer to external electrodes. Therefore, it is necessary for us to fully understand the dynamics of the band edge carriers

in $CuInS_2$ QDs and the way to transfer the photo-generated charges from $CuInS_2$ QDs to the external electrodes for best performance of the solar cells.

Recently, it had been demonstrated that the radiative recombination in $CuInS_2$ QDs involves a transition associated with the localized intragap state,[9,10] since it showed the long emission-lifetimes as well as the large Stokes-shift between the photoluminescence (PL) band and the band-edge absorption in $CuInS_2$ QDs. However, the band-edge-carrier dynamics in $CuInS_2$ QDs is ambiguous, leading to be unable to clarify the origin of the PL in $CuInS_2$ QDs. It is because the radiative recombination in $CuInS_2$ QDs does not come from the band-edge transitions. Instead the transient absorption spectra are dominated by filling of the lowest 1S quantized levels. Therefore, the dynamics of the band-edge carriers such as the 1S electron trapping at the surface defects can be well resolved in transient absorption spectra.

In $CuInS_2$-TiO_2 donor-acceptor systems, the electron transfer from $CuInS_2$ QDs is energetically allowable because the lowest unoccupied molecular orbital (LUMO) level of the porous anatase TiO_2 films is lower than the LUMO level in bulk $CuInS_2$. From Marcus theory,[16] the electron transfer rate is determined by the electronic coupling strength (H_{DA}), the total reorganization energy (λ), and the driving force energy (ΔG). In donor-acceptor hybrid systems of CdSe[17–19], CdS[20], and PbS[21] QDs coupling to TiO_2 or ZnO, the effects of three parameters above on the electron transfer dynamics have been explored widely. It was reported that both the electron and hole energies as well as the surface densities increase with decreasing QDs size, which increases the rate of both the charge transfer and charge trapping at the QD surface in QDs-TiO_2 systems. Therefore, it remains difficult to optimize the overall charge separation efficiency by selectively and rationally controlling the competing processes in core QDs.

The advancement in the synthesis of colloidal QDs has led to the preparation of more sophisticated core/shell QDs with multiple component materials and shapes that can be

tuned for desired functions. The $CuInS_2$ based semiconductor materials have been extensively tailored and combined into spherical core/shell QDs.[9, 14] By tailoring the potential energy profile through material choice and degree of quantum confinement via the size and the shape of the components, the electron and hole wavefunctions in $CuInS_2$ QDs can be engineered to control the photophysical properties, including energy levels, PL quantum yield, and the lifetimes of excitons. The $CuInS_2$ QDs have been engineered to exhibit type I carrier localization by coating ZnS shells and quasi-type II carrier localization by coating CdS shells.[9] This gives us the opportunities to optimizing the solar energy conversion by controlling interfacial charge separation processes through wavefunction engineering in $CuInS_2$ QDs.

Early $CuInS_2$ QDSSCs showed a power conversion efficiency of less than 1%.[22] Recently, the charge recombination at TiO_2/QD/electrolyte interfaces was suppressed by introducing the buffer layer and the efficiency of $CuInS_2$ QDSSCs were increased to 2.52%.[23–25] The Teng group further improved the $CuInS_2$ QDSSCs by optimizing the CdS passivation layer and achieved a power conversion efficiency of 4.2%.[26] The trap states at the interface or the surface of the QDs play a crucial role in degrading the performance of the QDSSCs. Although the defects at the interface or the surface of the QDs can be effectively passivated by CdS or ZnS layers, the actual power conversion efficiency of the QDSSCs is far below the theoretical value. The origin of such limited performance was ascribed to the poor charge transfer from $CuInS_2$ QDs to external electrodes. The charge transfer from $CuInS_2$ QDs is the primary event leading to photocurrent generation in QDSSCs. As we discussed above, we can optimize the charge transfer process from $CuInS_2$ QDs by means of wave function engineering in core/shell $CuInS_2$ QDs for best performance of the $CuInS_2$ QDSSCs.

In this thesis, we have studied the ultrafast carrier dynamics in $CuInS_2$ QDs and the electron transfer process from $CuInS_2$/ZnS core/shell quantum dots into TiO_2 films. Fi-

nallly, the QDSSCs consisting of a TiO_2 films sensitized with $CuInS_2$ QDs was fabricated.

This paper consists of the following chapters. In chapter 2, the synthesis method of $CuInS_2$ QDs is explained. The ultrafast carrier dynamics in $CuInS_2$ QDs is described in chapter 3. In chapter 4, the electron transfer process from $CuInS_2$/ZnS core/shell quantum dots into porous anatase TiO_2 films is investigated and written. In chapter 5, the fabrication of the QDSSCs is described and the effect of the band alignment on performance of the QDSSCs is discussed. The conclusion is given in chapter 6.

Bibliography

[1] W. U. Huynh, J. J. Dittmer and A. P. Alivisatos, Science **295**, 2425 (2002).

[2] A. J. Nozik, Phys. E. **14**, 115 (2002).

[3] P. V. Kamat, J. Phys. Chem. C. **112**, 18737 (2008).

[4] G. Hodes, J. Phys. Chem. C. **112**, 17778 (2008).

[5] R. D. Schaller and V. I. Klimov, Phys. Rev. Lett. **92**, 186601 (2004).

[6] M. Shalom, I. Hod, Z. Tachan, S. Buhbut, S. Tirosh and A. Zaban, Energy Environ. Sci. **4**, 1874 (2011).

[7] S. H. Im, H. J. Kim, S. W. Kim, S. W. Kim and S. I. Seok, Energy Environ. Sci. **4**, 4181 (2011).

[8] S. Shockley and H. J. Queisser, J. Appl. Phys. **32**, 510 (1961).

[9] L. Li, A. Pandey, D. J. Werder, B. P. Khanal, J. M. Pietryga, and V. I. Klimov, J. Am. Chem. Soc. **133**, 1176 (2011).

[10] H. Zhong, S. S. Lo, T. Mirkovic, Y. Li, Y. Ding, Y. Li, and G. D. Scholes, ACS Nano. **4**, 5253 (2010).

[11] W. S. Song and H. Yang, Appl. Phys. Lett. **100**, 183104 (2012).

[12] B. Chen, H. Zhong, W. Zhang, Z. Tan, Y. Li, C. Yu, T. Zhai, Y. Bando, S. Yang, and B. Zou, Adv. Funct. Mater. **229**, 2081 (2012).

[13] J. Zhang, R. Xie, and W. Yang, Chem. Mater. **23**, 3357 (2011).

[14] W. Zhang and X. Zhong, Inorg. Chem. **50**, 4065 (2011).

[15] X. Tang, W. Cheng, E. S. G. Choo, and J. Xue, Chem. Commun. **47**, 5217 (2011).

[16] R. A. Marcus, J. Chem. Phys. **24**, 966 (1956).

[17] K. Tvrdya, P. A. Frantsuzovc, and P. V. Kamat, Proc. Natl. Acad. Sci. **108**, 29 (2011).

[18] H. Zhu, N. Song, and T. Lian, J. Am. Chem. Soc. **132**, 15038 (2010).

[19] A. Kongkanand, K. Tvrdy, K. Takechi, M. Kuno, and P. V. Kamat, J. Am.Chem. Soc. **130**, 4007 (2008).

[20] D. F, Waton, J. Phys. Chem. Lett. **1**, 2299 (2010).

[21] B. R. Hyun, A. C. Bartnik, J. K. Lee, H. Imoto, L. Sun, J. J. Choi, Y. Chujo, T. Hanrath, C. K. Ober, and F. W. Wise, Nano Lett. **10**, 31 (2010).

[22] K. T. Kuo, D. M. Liu, S. Y. Chen and C. C. Lin, J. Mater. Chem. **19**, 6780 (2009).

[23] J. Y. Chang, L. F. Su, C. H. Li, C. C. Chang and J. M. Lin, Chem. Commun. **48**, 4848 (2012).

[24] G. P. Xu, S. L. Ji, C. H. Miao, G. D. Liu and C. H. Ye, J. Mater. Chem. **22**, 4890 (2012).

[25] T. L. Li, Y. L. Lee and H. S. Teng, J. Mater. Chem. **21**, 5089 (2011).

[26] T. L. Li, Y. L. Lee and H. S. Teng, Energy Environ. Sci. **5**, 5315 (2012).

Chapter 2

Synthesis and characterization of CuInS$_2$ quantum dots

2.1 Introduction

Cadmium and lead based quantum dots (QDs) have toxicity. Some researchers have turned their attention to ternary lower toxic I-III-VI$_2$ compounds such as CuInS$_2$ QDs.[1–14] The CuInS$_2$ QDs have attracted largest research interest to date among all ternary and quaternary QDs. In the past few years, a lot of synthesis methods have been developed for CuInS$_2$ QDs, such as heating-up[1–10] and hot-injection techniques[11–14].

It is known that the key to synthesizing monodisperse ternary QDs is to balance the reactivity of the two cationic precursors by their ligands, solvent matrix composition, and reaction temperature. For example, the 1-dodecanethiol can be used to tune the reactivity of the Cu precursor for synthesis of I-III-VI$_2$ QDs.[1,5,6,9] The 1-dodecanethiol can simultaneously play a role in stabilizing ligand and the solvent. It can further act as a sulfur source, because it forms thiolates with various metal salts, and because thiolates decompose to form the corresponding metal sulfides during heating. The copper iodide

and indium acetate reacted and eventually complexed with 1-dodecanethiol at $180-270°C$ yielding $CuInS_2$ QDs in the sub-10 nm range. The exciton Bohr radius in $CuInS_2$ is around 5 nm and is closed to the size of $CuInS_2$ QDs.[3] The larger QDs can be obtained by increasing the reaction time. This is probably due to the further decomposition of 1-dodecanethiol. Furthermore, this simple synthetic approach leads to the nearly complete consumption of the cationic precursors and high reaction yields.

Recently, the noninjection thermal decomposition route had been well developed for the synthesis of $CuInS_2$ QDs.[1–10] The energy-tunable absorption and emission spectra of $CuInS_2$ QDs was observed. A similar method has also been successfully employed by Li et al.[1] in the synthesis of $CuInS_2$ QDs. However, the resulting $CuInS_2$ QDs exhibited poor crystallinity and a large size distribution. In their current work, this synthetic method is further refined to give high quality monodisperse $CuInS_2/CdS$ and $CuInS_2/ZnS$ core/shell QDs in a high quantum yield.[2] The well-developed synthesis of $CuInS_2$ QDs gives the access to a large variety of theoretical studies, giving further insight into the potential applications of these QDs.

2.2 Synthesis of CuInS$_2$ quantum dots

2.2.1 Chemical materials

Indium(III) acetate (In(Ac)3, 99.99%), purchased from Sigma-Aldrich

Copper(I) iodide (CuI, 99.5%) purchased from Wako

1-dodecanethiol (DDT, 98%), purchased from Sigma-Aldrich

Zinc stearate (ZnSt2, technical grade), purchased from Sigma-Aldrich

Cadmium oxide (CdO, 99.99%) purchased from Sigma-Aldrich

1-octadecene (ODE, 90%), purchased from Sigma-Aldrich

1-oleic acid (OA, 90%), purchased from Sigma-Aldrich

All chemicals were used as purchased and without further purification.

2.2.2 Synthesis procedure

In a typical synthesis of $CuInS_2$ QDs, 1 m mol indium acetate was mixed with 1 m mol copper iodide and 10 mL 1-dodecanethiol in a three-necked flask. The mixture was degassed under vacuum for 5 min and purged with argon for three times. Then the flask was heated up to 120 °C for 20 min until a clear solution was formed. The temperature was then raised to 230 °C and maintained at that temperature for 1−45 min for growth of the different-sized $CuInS_2$ QDs. As the temperature increases, the color of the reaction solution progressively changed from colorless to green, yellow, red, and finally black, indicating nucleation and subsequent growth of $CuInS_2$ QDs. At the desired size, the reaction was quenched by immersing the flask in ice bath. The samples were purified three times with acetone and finally dispersed into toluene for storage.

Furthermore, the $CuInS_2$ core QDs were coated with shell of ZnS or CdS to form core/shell QDs by successive ionic layer absorption and reaction (SILAR) methods.[12] The precursors of Cd and Zn were prepared in advance. The zinc precursor was prepared by mixing of 2 m mol Zinc stearate and 20 mL 1-dodecanethiol and the mixture was heated up to 100 °C until the solution turned to clear. The cadmium precursor prepared by a mixing of 2 m mol cadmium oxide, 5 mL 1-oleic acid and 15 mL 1-octadecene and the mixture was heated up to 255 °C under argon until the solution turned to clear. Then 5 mL crude $CuInS_2$ solution diluted with 5 mL 1-dodecanethiol was loaded in a three-necked flask. The solution was degassed under vacuum for 5 min and purged with argon for three times. The solution was heated up to 240 °C. The 5 mL zinc precursor (cadmium precursor) was added dropwise into the reaction solution at 240 °C and the temperature was kept at 240 °C for 30 min for the growth of the ZnS or CdS shells. The shell growth was repeated to obtain the different-thickness shell on the $CuInS_2$ core QDs.

After the shell growth, the reaction was quenched by immersing the flask into ice bath. The samples were purified three times using hexane/acetone and finally dispersed into toluene for storage.

2.3 Characterization of CuInS$_2$ quantum dots

2.3.1 Optical properties

Photoluminescence (PL) spectra were recorded by a JASCO F-8500 spectrophotometer. Steady-state absorption spectra were recorded on a UV-vis-NIR scanning spectrophotometer (Hitachi U-3300). Time resolved PL was measured by means of time-correlated single photon counting (TCSPC) system coupled to a JASCO CT-25 monochromator and visible photomultiplier. The samples were excited at 375 nm using a 70 ps pulsed diode lasers (Hamamatsu PLP-10). Time resolution of the TCSPC system was about 1 ns.

It is known that the optical properties of QDs depend on their size, composition and surface states. The absorption spectra of CuInS$_2$ QDs were measured at room temperature and are shown in Fig. 2.1(a). A broad absorption band for all the samples is observed together with an absorption tail at long wavelength. Similarly to previous reports,[2,3] no sharp absorption peak was observed for any of the samples. The absorption edge gradually shifts toward longer wavelength with increasing the diameter of the QDs, in consistent with quantum confinement effect.

The PL spectra of CuInS$_2$ QDs were measured and shown in Fig. 2.1(b). Like previous reports,[2,3] the CuInS$_2$ QDs have a very broad PL band with the full width at half maximum (FWHM) of more than 100 nm. It was observed that the PL band gradually shifted to the longer wavelength in the NIR range with the increase of the diameters. Furthermore, emission peaks of the QDs exhibit a large Stokes shift of about 300 meV from their corresponding optical band gaps, indicating that the radiative transition does

not come from excitonic recombination.

After the shell growth, the average diameters of the QDs increased, as was observed in the transmission electron microscopy (TEM) images in Fig. 2.6. Both optical absorption and PL spectra of the $CuInS_2$/ZnS core/shell QDs were blue-shifted with respect to those of their parent $CuInS_2$ QDs, as shown in Fig. 2.2. It is likely indicative of etching of the core material under shell growth conditions. CdS overgrowth proceeded with a similar initial blue shift, as shown in Fig. 2.3(a), followed by a subsequent red shift; the latter is consistent with slight delocalization of the electron into the CdS layer, similarly to the report of Klimov group.[2] Either ZnS or CdS overcoating results in a dramatic improvement of the PL quantum yield, as shown in Fig. 2.3(b).

To understand the origin of the PL in $CuInS_2$ QDs deeply, the PL lifetimes of core/shell QDs were studied by means of time-resolved PL spectroscopy. It is found that the PL decay curves of as-prepared $CuInS_2$ QDs are multi-exponential in nature. The PL decay curves are devided into three decay components with the best fit. We attributed the fast decay time component to be the nonradiative recombination process at the surface defect states. As shown in Fig. 2.4, the PL lifetimes of the $CuInS_2$/ZnS core/shell QDs exhibit a significant increase compared with the bare $CuInS_2$ QDs, suggesting the improved passivation of surface defects in the QDs. Long PL decay components in the $CuInS_2$ QDs emission band have been previously attributed to surface traps.[3, 4] Our observation contradicts such an assignment. As shown in Fig. 2.3(a), the PL quantum yields increased with the improvement of surface passivation by ZnS-shell coating.

Compared to $CuInS_2$/ZnS core/shell QDs, PL lifetimes further increased in $CuInS_2$/CdS core/shell QDs, as shown in Fig. 2.4. This is because the overlapping of the wave function for electrons and holes reduces in $CuInS_2$/CdS core/shell QDs. The delocalization of the electron wave function from the core to the CdS shell was enhanced due to the lower conduction band offset between $CuInS_2$ and CdS.[2] As shown in schematic diagram in

Fig. 2.4, the CuInS$_2$ QDs are engineered to exhibit quasi-type II carrier localization by coating CdS shells.

2.3.2 Morphology and crystal structure

As shown in Fig. 2.5(a-c), the diameters of the three types of CuInS$_2$ core QDs were determined to be 2.5, 3.3, and 4.0 nm, respectively, by means of TEM. The powder X-ray diffraction (XRD) patterns shown in Fig. 2.5(e) were obtained from a Rigaku-2000 diffractometer emitting Cu-Kα radiation. The reflection peaks of CuInS$_2$ QDs at 28.5 degree, 47.4 degree, and 55.5 degree in 2θ can be assigned to (112), (220)/(204), and (312)/(116) planes of a tetragonal chalcopyrite structure of CuInS$_2$, in consistent with the selected area electron diffraction patterns shown in Fig. 2.5(d).

2.3.3 Electrochemical properties

The band gaps and energy levels of the QDs are important parameters for devices design and material selections in solar cells. Cyclic voltammetry has been proven to be an effective way to determine the bandgaps and the energy levels of the highest occupied molecular orbital (HOMO) and the lowest unoccupied molecular orbital (LUMO) of QDs.[3, 15] The oxidation process is related to the injection of a hole into the HOMO levels, and the reduction process is related to the injection of an electron into the LUMO levels. The energy levels can be calculated from the onset oxidation potential (E_{ox}) and onset reduction potential (E_{red}), respectively, according to the following equations

E_{HOMO} = -(E_{ox} + 4.71) eV,

E_{LUMO} = -(E_{red} + 4.71)eV,

where the unit of the potentials is V vs Ag/Ag$^+$ (0.01 M) reference electrode.

Cyclic voltammetric curves were recorded on a electrochemical workstation (Princeton Applied Research VersaSTAT 3). As shown in Fig. 2.7, we used a glassy carbon disk as

Table 2.1 The LUMO and HOMO levels of $CuInS_2$ QDs. The values of E_g were determined from cyclic voltammograms.

| Diameters of $CuInS_2$ QDs (nm)	LUMO (eV)	HOMO (eV)	E_g (eV)
2.5	-3.65	-5.76	2.11
3.3	-3.77	-5.74	1.97
4.0	-3.88	-5.73	1.85

the working electrode (W), a Pt plate as the counter electrode (C), and Ag/Ag^+ in 0.1 M tetrabutylammonium hexafluorophosphate ($TBAPF_6$) dissolved in acetonitrile as the reference electrode (R). $TBAPF_6$ was dissolved in acetonitrile (0.1 M) as the supporting electrolyte. A drop of the high concentration $CuInS_2$ QDs solution was placed on the surface of the working electrode and then the solvent was evaporated to form a film of QDs on the surface of the electrode. After measurement, the glassy carbon disk was first cleaned in hexane for about 5 min then in acetone for another 5 min and dried before the deposition of new samples.

The LUMO and HOMO energy levels of the $CuInS_2$ core QDs were obtained from cyclic voltammetric curves in Fig. 2.8. The resulting energy levels were summarized in Table 2.1 The energy of the HOMO levels decreases and the energy of the corresponding LUMO levels increases with the increase of the diameters, in consistent with quantum confinement effect.

Bibliography

[1] L. Li, T. J. Daou, I. Texier, T. Thi, K. Chi, N. Q. Liem and P. Reiss, Chem. Mater. **21**, 2422 (2009).

[2] L. Li, A. Pandey, D. J. Werder, B. P. Khanal, J. M. Pietryga, and V. I. Klimov, J. Am. Chem. Soc. **133**, 1176 (2011).

[3] H. Zhong, S. S. Lo, T. Mirkovic, Y. Li, Y. Ding, Y. Li, and G. D. Scholes, ACS Nano. **4**, 5253 (2010).

[4] H. Zhong, Y. Zhou, M. Ye, Y. He, J. Ye, C. He, C. Yang and Y. Li, Chem. Mater. **20**, 6434 (2008).

[5] W. S. Song and H. Yang, Appl. Phys. Lett. **100**, 183104 (2012).

[6] B. Chen, H. Zhong, W. Zhang, Z. Tan, Y. Li, C. Yu, T. Zhai, Y. Bando, S. Yang, and B. Zou, Adv. Funct. Mater. **22**, 2081 (2012).

[7] J. Zhang, R. Xie, and W. Yang, Chem. Mater. **23**, 3357 (2011).

[8] W. Zhang and X. Zhong, Inorg. Chem. **50**, 4065 (2011).

[9] X. Tang, W. Cheng, E. S. G. Choo, and J. Xue, Chem. Commun. **47**, 5217 (2011).

[10] X.Yuan, J. Zhao, P. Jing, W. Zhang, H. Li, L. Zhang, X. Zhong, and Y. Masumoto, J. Phys. Chem. C. **116**, 11973 (2012).

[11] M. Nam, S. Lee, J. Park, S.-W. Kim and K.-K. Lee, Jpn. J. Appl. Phys. **50**, 0602 (2011).

[12] J. Park and S.-W. Kim, J. Mater. Chem. **21**, 3745 (2011).

[13] H. Zhong, Z. Wang, E. Bovero, Z. Lu, F. C. J. M. Van Veggel and G. D. Scholes, J. Phys. Chem. C **115**, 12396 (2011).

[14] H. Zhong, Y. Y. Li, M. Ye, Z. Zhu, Y. Zhou and C. Yang, Nanotechnology **18**, 025602 (2007).

[15] B. R. Hyun, A. C. Bartnik, J. K. Lee, H. Imoto, L. Sun, J. J. Choi, Y. Chujo, T. Hanrath, C. K. Ober, and F. W. Wise, Nano Lett. **10**, 31 (2010).
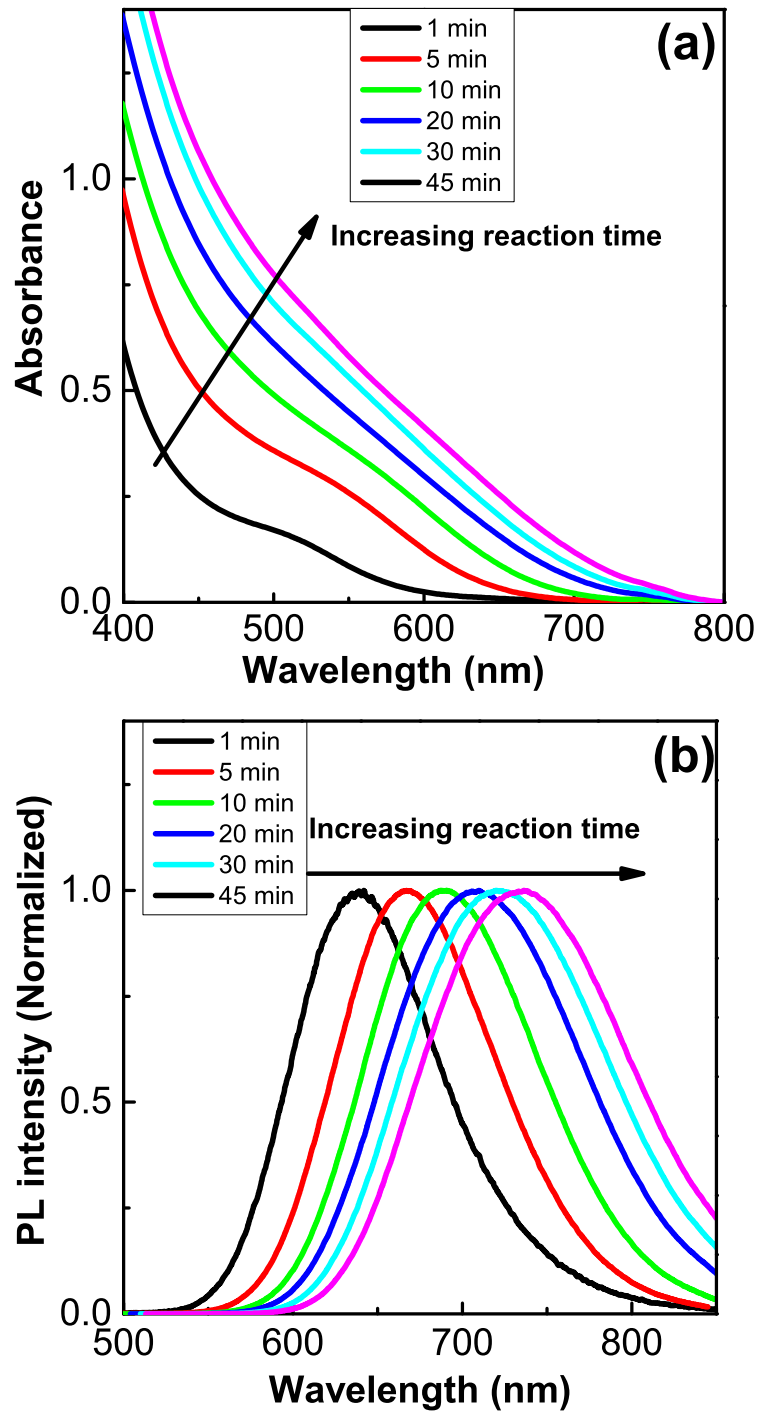
FIG. 2.1 (a) Absorption and (b) Photoluminescence (PL) spectra of CuInS$_2$ QDs with different reaction time at tempreture of 230 °C.
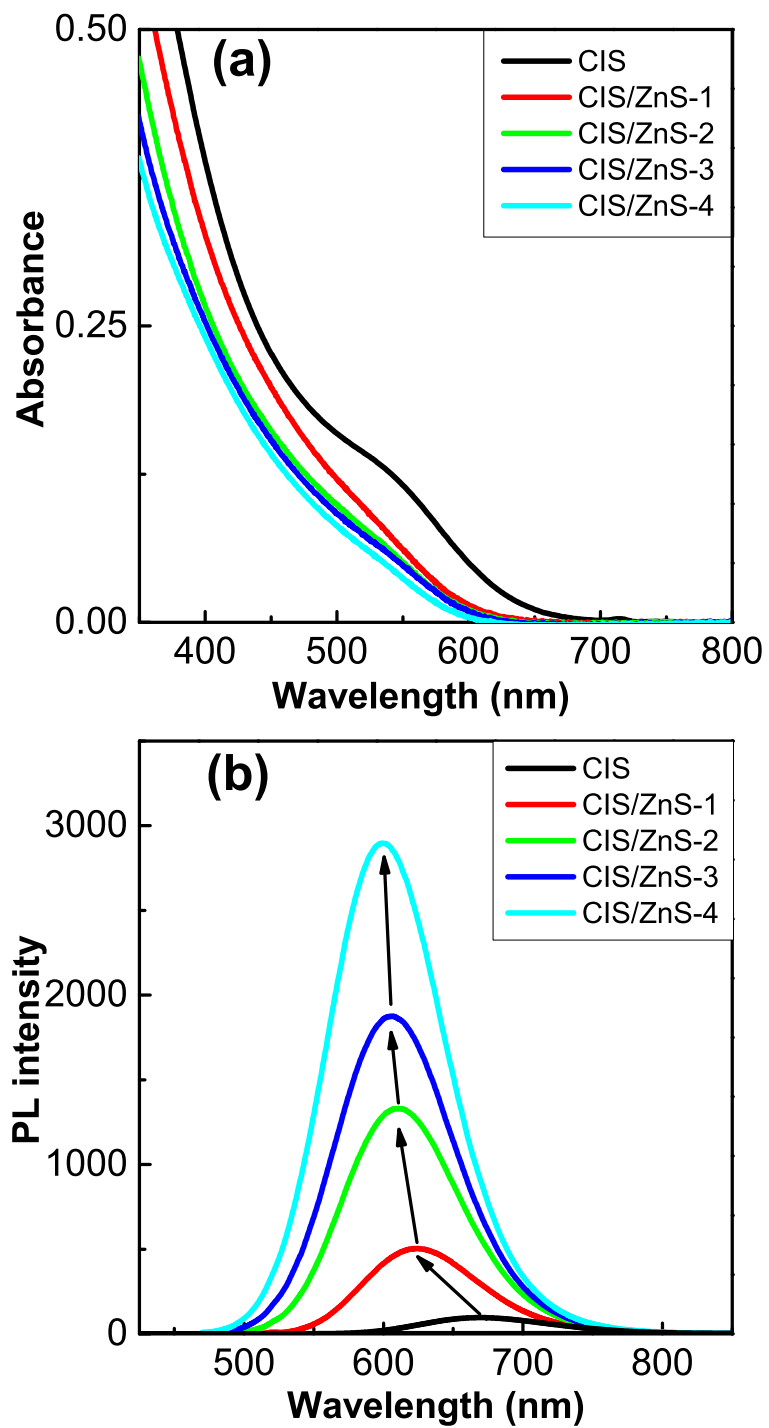
FIG. 2.2 (a) Absorption and (b) PL spectra of CuInS$_2$/ZnS core/shell QDs with increasing the shell thickness.
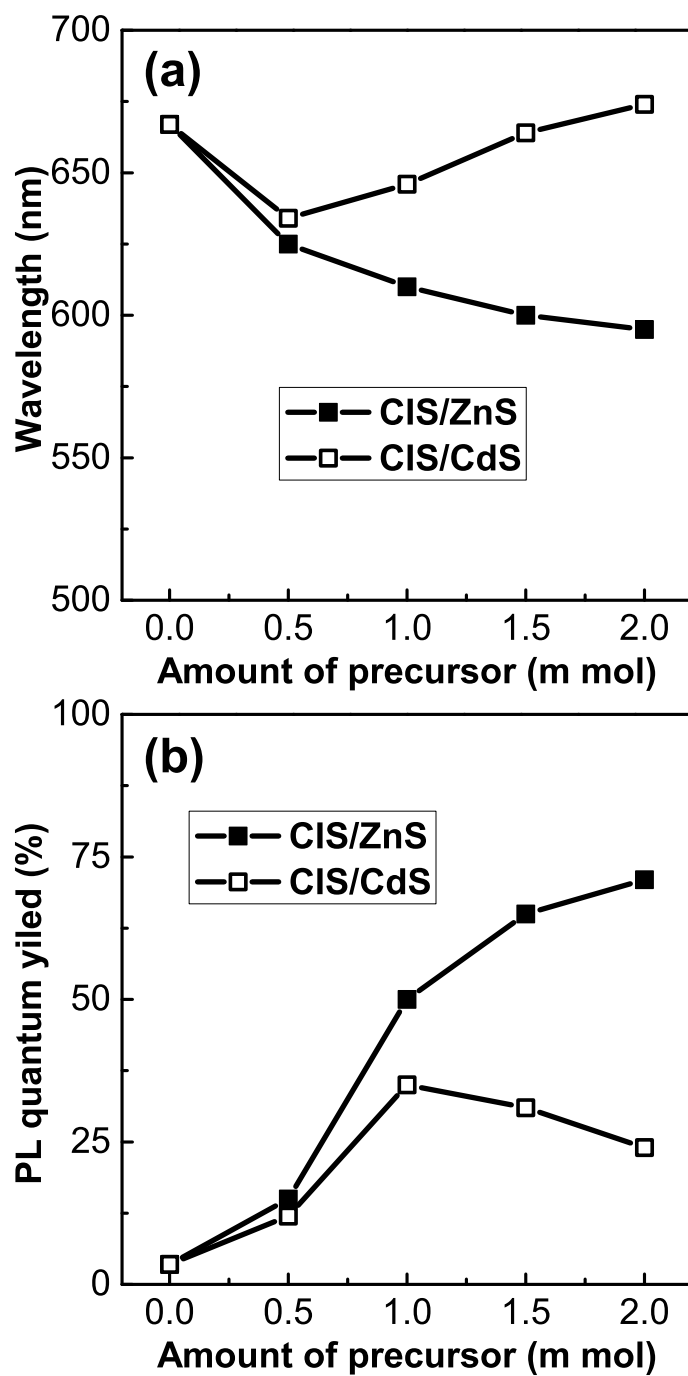
FIG. 2.3 (a) Photoluminescence peaks and (b) quantum yields of $CuInS_2/ZnS$ and $CuInS_2/CdS$ core/shell QDs as a function of the amount of precursor injected into the reaction.
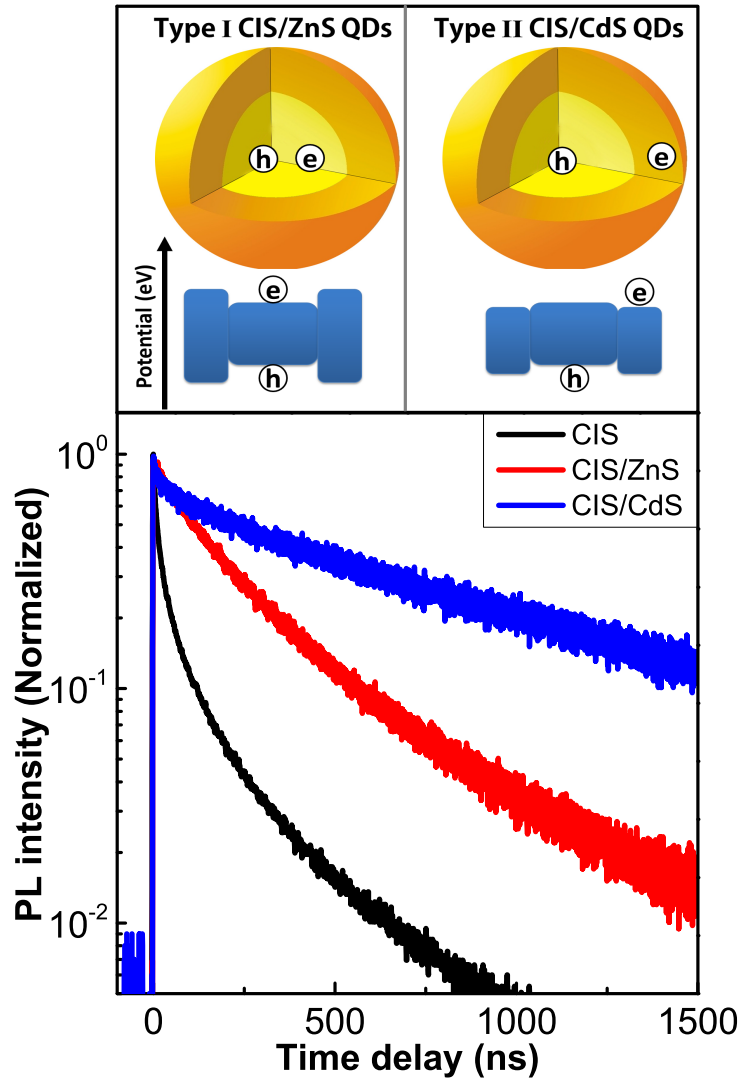
FIG. 2.4 Photoluminescence decay curves of the $CuInS_2$ QDs, $CuInS_2$ QDs/ZnS core/shell QDs and $CuInS_2$ QDs/CdS core/shell QDs. The delocalization of the electron wave function from core to CdS shell was enhanced due to the lower conduction band offset between $CuInS_2$ and CdS. The $CuInS_2$ QDs was synthesized to exhibit quasi-type II carrier localization by coating CdS shells.
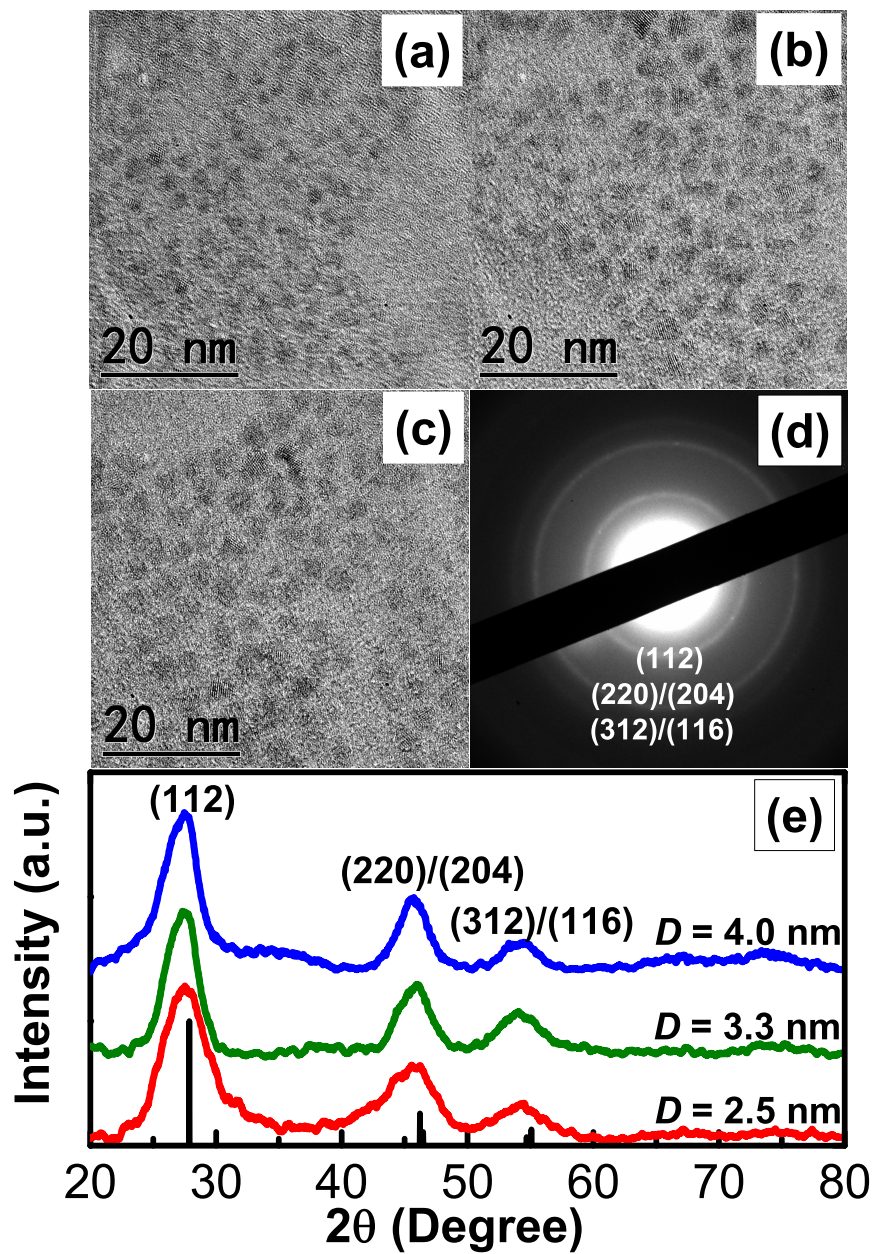
FIG. 2.5 Transmission electron microscopy (TEM) images for CuInS$_2$ QDs (a) 2.5 nm, (b) 3.3 nm and (c) 4.0 nm in diameter; (d) a typical selected area electron diffraction pattern and (e) powder X-ray diffraction patterns of CuInS$_2$ QDs.

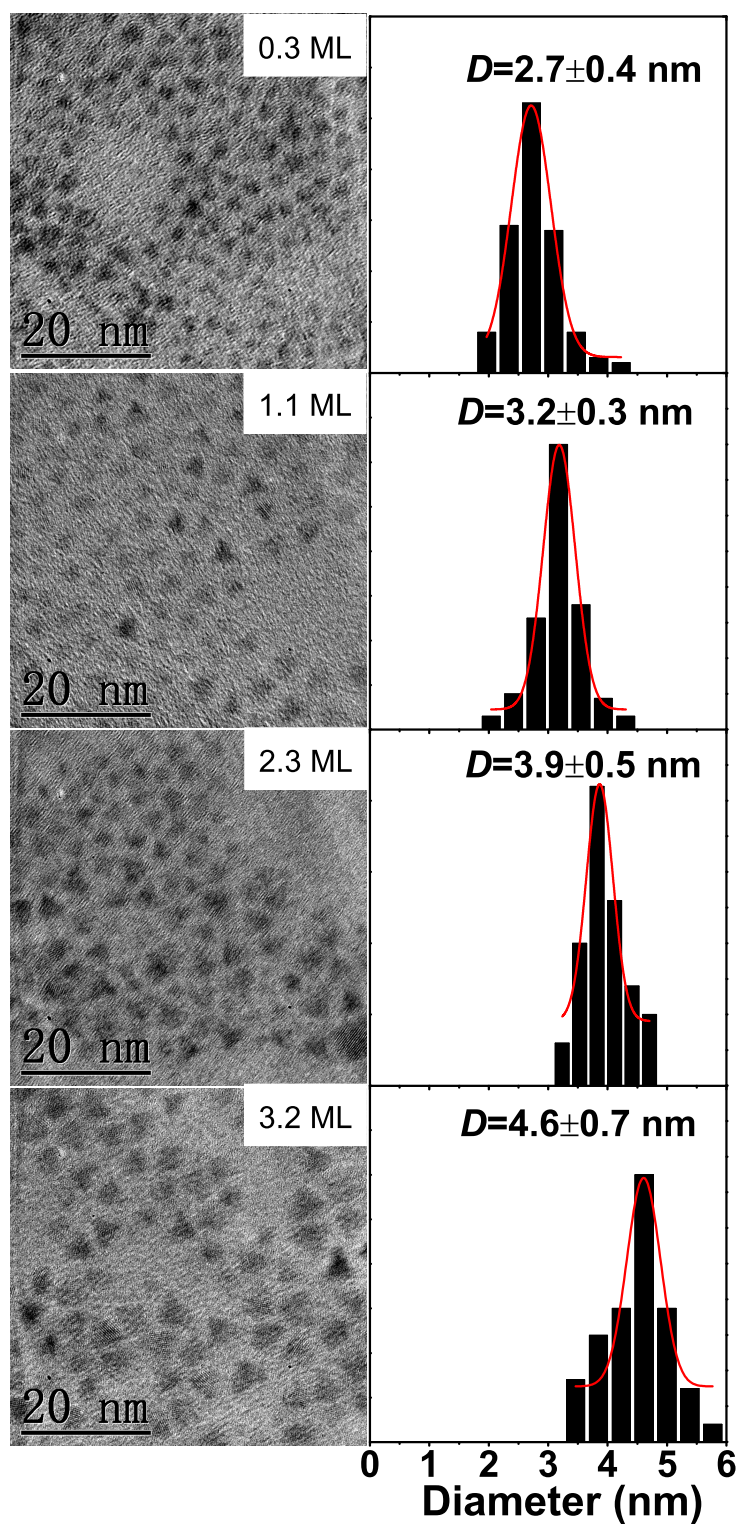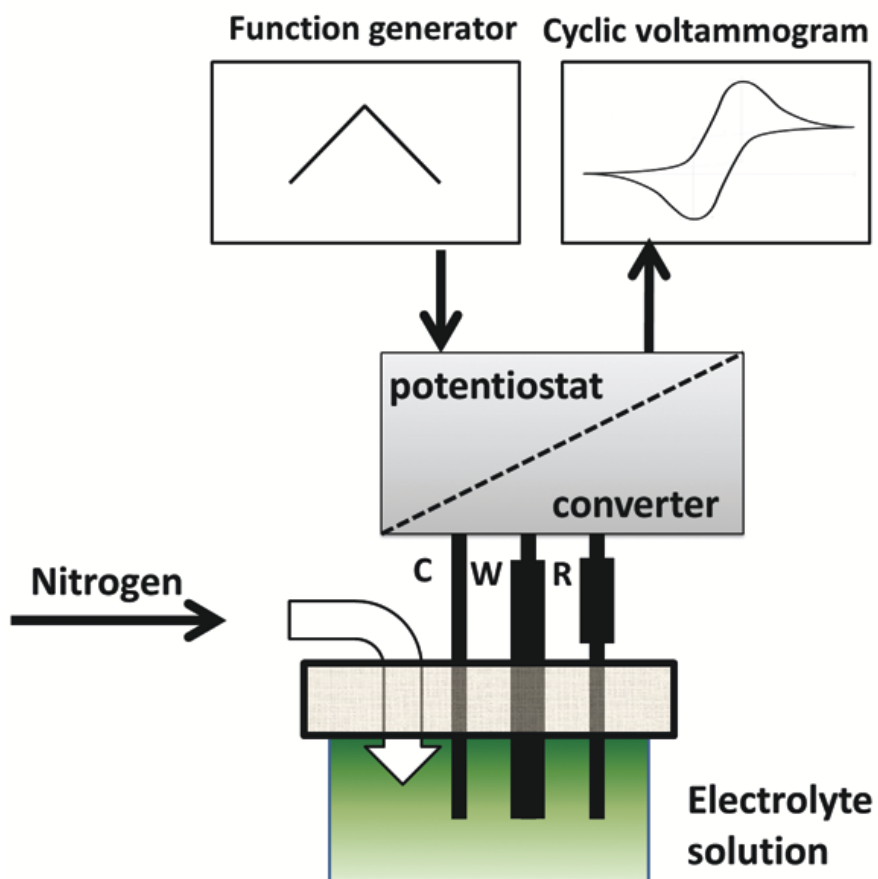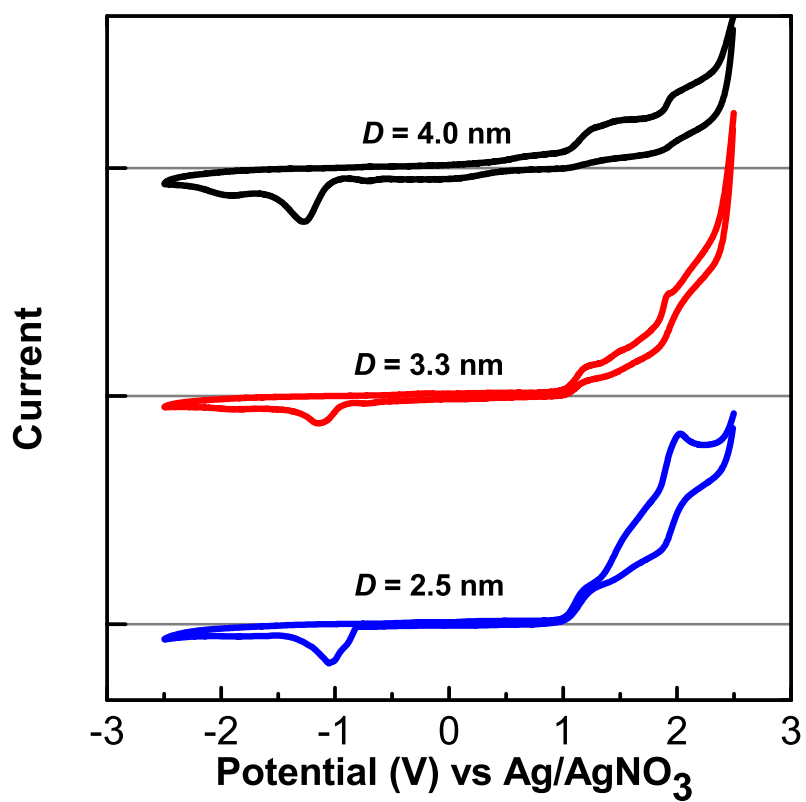**FIG. 2.6** Representative TEM images of CuInS$_2$/ZnS QDs with a core 2.5 nm in diameter.

FIG. 2.7 Schematic drawing of the cyclic voltammetry system.

FIG. 2.8 Cyclic voltammograms of three kinds of CuInS$_2$ QDs 2.8, 3.3 and 4.0 nm in diameter.

Chapter 3

Ultrafast carrier dynamics in CuInS$_2$ quantum dots

3.1 Introduction

Quantum dots (QDs) exhibit profound size-dependent optical and electronic properties, having attracted much interests in both fundamental science and applications to solar cells[1,2] and light emitting diodes.[3,4] The carrier relaxation in QDs is extremely sensitive to the surface characteristics due to the considerable surface-to-volume ratio. The defects on the QD surface such as the dangling bonds act as the trap states near the band edge. In most cases, carrier trapping at the surface defects takes place in less than 100 ps in CdS[5] and CdSe[6–9] QDs. The fast carrier-trapping significantly reduces the efficiency of the band-edge photoluminescence (PL). As alternatives to II-VI QDs, chalcopyrite-type I-III-VI$_2$ QDs have been proposed because of their less-toxic components. Among them, CuInS$_2$ QDs are important candidates for optoelectronic devices, because bulk CuInS$_2$ has a direct band gap of 1.53 eV.[10–13] Naturally, the ultrafast carrier dynamics in CuInS$_2$ QDs have become of great interest.

Recently, it has been demonstrated that the radiative recombination in $CuInS_2$ QDs involves a transition associated with the localized intragap state,[10,12] since it showed the long emission-lifetimes as well as the large Stokes-shift between the PL band and the band-edge absorption in $CuInS_2$ QDs. However, the band-edge-carrier localization by intragap states in $CuInS_2$ QDs is ambiguous, leading to be unable to clarify the origin of the PL in $CuInS_2$ QDs. It is because the radiative recombination in $CuInS_2$ QDs does not come from the band-edge transitions. The dynamics of the band-edge carriers can not be directly resolved in the time-resolved PL spectroscopy.[11,12] In contrast, the transient absorption (TA) spectra are dominated by filling of the lowest 1S quantized levels and the dynamics of the band-edge carriers such as the 1S electron trapping at the surface defects can be well resolved.

In this chapter, we investigated the mechanisms for optical nonlinearities and ultrafast carrier dynamics in $CuInS_2$ QDs by means of femtosecond TA spectroscopy. We observed a nearly symmetrical bleaching band and a broad photoinduced absorption (PA) region in the TA spectra. Furthermore, we measured the laser-intensity dependence of the TA to confirm that the band-edge bleach in $CuInS_2$ QDs is dominated by filling of 1S electron states. From the initial decay of the bleaching, the surface trapping of the 1S electrons had been studied in $CuInS_2$ core and $CuInS_2$/ZnS core/shell QDs.

3.2 Experimental

3.2.1 Sample preparation

We synthesized the $CuInS_2$ core and $CuInS_2$/ZnS core/shell QDs by a wet chemical method.[10] The average diameters of three kinds of $CuInS_2$ QDs were determined to be 2.5, 3.3, and 4.0 nm, respectively, by means of transmission electron microscopy (TEM). The QDs dispersed in toluene were sealed in quartz cells 1 mm thick for the measurements.
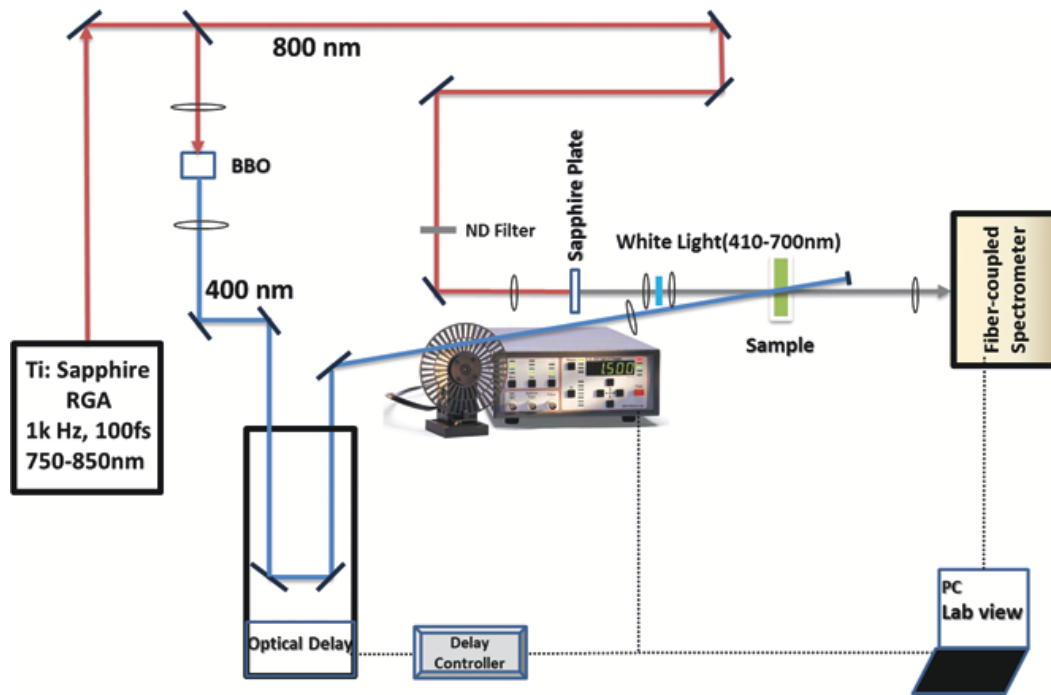
FIG. 3.1 Optical setup of the femtosecond transient absorption (TA) spectrometer.

3.2.2 Femtosecond transient absorption spectrometer

The white-light femtosecond TA spectrometer used in this study is based on a regeneratively amplified Ti:sapphire laser system (Spectra-Physics, 800 nm, 130 fs, and 1 kHz repetition rate). As shown in Fig. 3.1, pump pulses at 400 nm were generated by frequency doubling of the 800 nm laser beam in a BBO crystal 2 mm thick. The white-light probe was generated by focusing the 800 nm laser beam onto a sapphire plate 2 mm thick. The pump pulses were chopped by a synchronized chopper to 25 Hz. After the sample, the probe was focused into a fiber-coupled spectrometer (Ocean Optics USB2000+, 2048 pixel CCD, 300-1100 nm). The angle between pump and probe polarizations was set at magic angle (54.6 degree) to ensure the dynamics free from reorientation effects. The group velocity dispersion of the whole experimental system was compensated by a chirp program. During the data collection, samples were constantly moved in X−Y directions at a speed of 10 cm/min to avoid the degradation of the samples.

3.3 Experimental results and discussion

3.3.1 Optical nonlinearities in CuInS$_2$ quantum dots

The steady-state absorption, PL and TA spectra for CuInS$_2$ QDs grown at 230 °C are shown in Fig. 3.2. The absorption edge and PL band gradually shift toward longer wavelength with increasing the diameter of the QDs, in consistent with quantum confinement effect. Like previous reports,[10–12] no sharp excitonic absorption peak was observed in the steady-state absorption spectra. It is well known that the presence of discrete electronic states is masked in the linear absorption spectra by large inhomogeneous broadening in CuInS$_2$ QDs.[12, 14] Each QD may vary in size, geometry, and stoichiometry, especially for CuInS$_2$ QDs because of their ternary chemical-composition. These variations cause a strong inhomogeneous broadening of the optical transitions. In contrast, the structures of the 1S transition can be well resolved in nonlinear TA spectra, as shown by dash-dotted lines in Fig. 3.2. This is because the nonlinear TA spectra are dominated by bleaching of the 1S transitions after the fast intraband carrier relaxation is completed.

Furthermore, we calculated the band gaps, the lowest optical transition energy of CuInS$_2$ QDs on the finite-depth-well model in the effective mass approximation. The effective masses of electrons and holes are $0.16m_0$ and $1.30m_0$, respectively, where the m_0 is the electron mass in vacuum.[12] As shown in Fig. 3.3, size-dependent 1S transition energy determined from bleaching spectra is in agreement with that calculated. On the other hand, the emission peak deviates from its corresponding band gap calculated, and the deviation, that is Stokes shift, increases up to 0.38 eV with the decrease in the size of CuInS$_2$ QDs. Besides, it was reported that the radiative recombination in CuInS$_2$ QDs showed the long emission-lifetime of more than 300 ns.[10, 19] This suggests that the radiative recombination does not come from band-edge transition.

We investigated the laser-intensity dependence of the TA to understand the intrinsic

characters of the carrier in CuInS$_2$ QDs. Two features are observed in the TA spectra presented in Fig. 3.4: a rather symmetrical bleaching band and a broad PA region extending to low-energy side in the spectra. The bleaching of 1S transitions increases with the increase of pump fluence. As shown in Fig. 3.5, the bleaching saturated at higher fluence indicates that the number of states of 1S transitions is finite in CuInS$_2$ QDs. It had been suggested that the band-edge bleach at room temperature is dominated by filling of 1S electron states without a discernible contribution from holes in CuInS$_2$ QDs.[10] This is because the degeneracy of the valence band is much larger than that of the conduction band, which is a combined result of the large difference between electron and hole masses ($m_h/m_e = 8$) and the multiband structure of the valence band in CuInS$_2$.

When the pump-photon energy (3.1 eV) is much higher than the band gap of QDs so that the saturation at the pump wavelength is insignificant, the populations in the QDs following the Poisson distribution: $P(N) = \langle N \rangle^N e^{-\langle N \rangle}/N!$ can be calculated, where $P(N)$ is the probability of having N electron-hole pairs in a dot in case the average populations of QDs are $\langle N \rangle$.[8, 15] The 1S absorption change (ΔA) is proportional to the population of the 1S electron state. It can be expressed as $\Delta A \propto \langle n_{1S} \rangle$, where $\langle n_{1S} \rangle$ is the average occupation number of the 1S electron state. Because of the twofold spin degeneracy for the 1S electron state shown in the inset in Fig. 3.5, $\langle n_{1S} \rangle$ can be calculated as: $\langle n_{1S} \rangle = 1 - e^{-\langle N \rangle}(1 + \langle N \rangle/2)$.[15] At the initial stage ($\Delta t = 4$ ps) of the 1S electron relaxation, $\langle N \rangle$ is directly proportional to the pump fluence (j_p) and can be expressed as: $\langle N \rangle = j_p \sigma_a$,[16] in which the σ_a is the absorption cross section of a QD at the excitation wavelength of 400 nm.[17] Therefore, we obtain the following expression:[8, 15, 17]

$$\langle n_{1S} \rangle = 1 - e^{-j_p \sigma_a}(1 + j_p \sigma_a/2). \tag{3.1}$$

The pump-fluence-dependent changes of the 1S absorption can be well fitted by Eq. (3.1).

As seen in Fig. 3.5, the data show the initial linear growth followed by saturation similarly to the behavior observed in CdSe QDs.[8, 15] The fitting yields σ_a of 3.9×10^{-16} (cm^2), which is comparable to the calculated value of 3.5×10^{-16} (cm^2) for a 2.5 nm CuInS$_2$ QD at the wavelength of 400 nm.[10] The good fit confirms that the band-edge bleach in CuInS$_2$ QDs is dominated by filling of 1S electron states.

The PA observed in QDs is associated with either the Coulomb multiparticle interactions, such as the biexciton effect[8, 14] or the trapped-carrier related excited-state absorption[15]. Although the ground biexciton states can be formed in CuInS$_2$ QDs, the sharp biexcitonic features are not observed probably due to the broadening of the 1S bleach band. As shown in Fig. 3.4, there is little wavelength selectivity in the spectra of PA of CuInS$_2$ QDs. Moreover, the PA signals show the linear growth with the pump fluence and do not show saturation as shown by hollow squares in Fig. 3.5. Therefore, the spectrally-broad PA observed in CuInS$_2$ QDs most likely originates from the transition of carriers trapped at defect states. Furthermore, the PA observed in well-passivated CuInS$_2$/ZnS core/shell QDs indicated that carriers are trapped even inside the CuInS$_2$ QDs, in consistent with the recent report claiming the internal defect states stem from the substitution of the copper and indium ions in CuInS$_2$ QDs.[10]

3.3.2 Ultrafast carrier dynamics in CuInS$_2$ quantum dots

It is an important concern that a high probability of the carrier trapping at surface defects degenerates the performance of QD-based optoelectronic devices.[10, 18, 19] It was found that the low efficiency of the electron injection into TiO$_2$ films from small CuInS$_2$ QDs was attributed to the large amount of surface-localized states.[19] Recently, the carrier trapping in CuInS$_2$ QDs has been studied mainly by means of time-resolved PL spectroscopy.[10–13] These reports show that the luminescence of the CuInS$_2$ QDs is significantly reduced due to the surface trapping effects. However, it is unable to distinguish

electron and hole trapping at the trap states in the time-resolved PL spectroscopy, because both electrons and holes contribute to the PL dynamics.[8] As discussed above, the TA spectra are dominated by filling of 1S electron states after the intraband relaxation. Therefore, we can use the 1S bleaching decay dynamics to evaluate the depopulation rate of the 1S electrons in $CuInS_2$ QDs. The 1S electron relaxation paths in $CuInS_2$ QDs can be clearly revealed.

For all the decay curves shown in Fig. 3.6, the TA kinetics can not be fitted by a single-exponential decay. The TA kinetics show two distinct regions: the initial fast decay in sub-100-ps followed by slow nanosecond decay. A quantitative analysis of the decay curves was carried out by a simple bi-exponential fit. The initial decay in sub-100-ps as well as the corresponding signal decrease is sensitive to the size of the $CuInS_2$ QDs. In smallest $CuInS_2$ QDs, the population of 1S electron decreases quickly at a time constant of 14 ps by 23% of the initial peak amplitude followed by slow decrease at a time constant of 1.8 ns by 77% of the initial peak amplitude. The TA measurement was performed in the low-intensity excitation regime (average number of absorbed photons equals to 0.5) where the fast multiparticle Auger recombination was insignificant.[7,8] The initial 14 ps decay is most likely due to the electron relaxation from the 1S state to a new state, such as the surface-defect state in the band gap. The inset in Fig. 3.6 shows a plot of initial-decay rate ($1/\tau_i$) as a function of the average radius (R). The initial-decay rates slow markedly as the QD radius increases. The solid line in the inset in Fig. 3.6 shows the best fit of these data by a power-law expression: $1/\tau_i = CR^n$, where C is a constant and n describes the order. The fitting yields n of -1.8, which is comparable to the reported one (-1.5) for CdSe QDs.[20] The electron capture rate at the surface of $CuInS_2$ QDs was evaluated to explain the relationship between QDs radius and the initial-decay rate. The details of the calculation were described previously.[19] As shown in the inset in Fig. 3.6, the calculated radial electron densities at the QD surface as a function of QD radius

follow the size dependence of $R^{-1.6}$, in reasonable agreement with the size dependence of the initial-decay rate of $R^{-1.8}$. The agreement with the calculation indicates that the initial-decay rate is proportional to the existing probability of electron at the QD surface. Therefore, the initial decay in sub-100-ps in $CuInS_2$ QDs is due to the electron relaxation from the 1S state to the surface-defect state.

We further investigated the 1S electron trapping at the defects by making ZnS shells on $CuInS_2$ core QDs. After overcoating with ZnS, the quantum yield of PL increased from 3.5% in the core QDs to 81% in the $CuInS_2$/ZnS core/shell QDs. The significant increase in efficiency of the band-edge PL indicates that the surface defects in bare QDs are effectively passivated by ZnS shells. As seen in Fig. 3.7, the bleaching in $CuInS_2$/ZnS core/shell QDs recovers extremely slowly in contrast with the fast recovery of the bleaching in $CuInS_2$ core QDs. The initial-decay time increased up to 91 ps with a small decay amplitude of 1.3%. The improvement in surface passivation leads to the suppression of the fast decay component, confirming that the fast decay component comes from electrons trapping at surface defects. However, the PA is observed at the lower energy side of the bleaching band in well-passivated $CuInS_2$/ZnS core/shell QDs, as shown in Fig. 3.8. The observed PA in $CuInS_2$/ZnS core/shell QDs originates from the transition of carriers trapped at internal defects. Besides, the 1S bleaching spectra show the red shift (about 10 nm) as the time proceeds in $CuInS_2$ core QDs. This indicates that the different relaxation behavior is associated with a size inhomogeneity in $CuInS_2$ core QDs. The relaxation of the 1S electrons is faster in smaller QDs with larger density of electrons at surface.

The PL in $CuInS_2$ QDs had been previously attributed to the recombination of donor-acceptor pairs.[13] In recombination of donor-acceptor pairs, the electrons and holes at the band edge are fast trapped by the donors (about 10-20 ps) and the acceptors (within 1 ps), respectively, and then the trapped electron-hole pairs recombine to emit photons.[5] However, we observed that the electrons in $CuInS_2$/ZnS QDs are not localized. Our

observation contradicts with the previous report which claimed that the PL in $CuInS_2$ QDs comes from the recombination of donor-acceptor pairs. The localized carrier in $CuInS_2$ QDs must be the hole. The long-lifetime emission is most entirely involved with the transition from a 1S electron state to a hole-localized state.

3.4 Conclusions

In summary, we have investigated the mechanisms for optical nonlinearities and ultra-fast carrier dynamics in $CuInS_2$ QDs by means of femtosecond TA spectroscopy. The size-dependent 1S transition energy was obtained from bleaching spectra in agreement with the calculated one. From pump-intensity dependence of the TA spectra, we found that the 1S absorption changes as a function of pump fluence could be well fitted on the state-filling model. In state-filling model, the population of electrons follows the Poisson distribution. Therefore, the TA bleaching in $CuInS_2$ QDs is dominated by filling of the 1S electron states. Based on such a verdict, the ultrafast electron dynamics was investigated in $CuInS_2$ QDs. The decay in sub-100-ps is due to the electron relaxation from the 1S state to a surface-defect state. We found that the sub-100-ps electron trapping in bare QDs accelerated with decreasing QDs size. The rates of the electron trapping were shown to scale with the inverse of QD radius ($1/\tau_i \propto R^{-1.8}$). These surface trapping states were effectively passivated in $CuInS_2/ZnS$ core/shell QDs. The experimental results clearly show the intrinsic characters of the 1S electron states in $CuInS_2$ QDs and the way to further optimize the $CuInS_2$ QDs-based optoelectronic devices.

Bibliography

[1] W. U. Huynh, J. J. Dittmer, and A. P. Alivisatos, Science **295**, 2425 (2002).

[2] I. Gur, N. A. Fromer, M. L. Geier, and A. P. Alivisatos, Science **310**, 462 (2005).

[3] S. Coe, W. K. Woo, M. Bawendi, and V. Bulović, Nature **420**, 800 (2002).

[4] J. L. Zhao, J. A. Bardecker, A. M. Munro, M. S. Liu, Y. H. Niu, I. K. Ding, J. D. Luo, B. Q. Chen, A. K.-Y. Jen, and D. S. Ginger, Nano Lett. **6**, 463 (2006).

[5] V. I. Klimov, P. H. Bolivar, and H. Kurz, Phys. Rev. B **53**, 1463 (1996).

[6] V. I. Klimov and D. W. McBranch, Phys. Rev. Lett. **80**, 4028 (1998).

[7] V. I. Klimov, A. A. Mikhailovsky, D. W. McBranch, C. A. Leatherdale, and M. G. Bawendi, Science **287**, 1011 (2000).

[8] V. I. Klimov, J. Phys. Chem. B **104**, 6112 (2000).

[9] P. T. Jing, W. Y. Ji, X. Yuan, M. Ikezawa, L. G. Zhang, H. B. Li, J. L. Zhao and Y. Masumoto, J. Phys. Chem. Lett. **4**, 2919 (2013).

[10] L. Li, A. Pandey, D. J. Werder, B. P. Khanal, J. M. Pietryga, and V. I. Klimov, J. Am. Chem. Soc. **133**, 1176 (2011).

[11] X. Yuan, J. L. Zhao, P. T. Jing, W. Zhang, H. B. Li, L.G. Zhang, X. H. Zhong and Y. Masumoto, J. Phys. Chem. C. **116**, 11973 (2012).

[12] H. Zhong, S. S. Lo, T. Mirkovic, Y. Li, Y. Ding, Y. Li, and G. D. Scholes, ACS Nano. **4**, 5253 (2010).

[13] B. Chen, H. Zhong, W. Zhang, Z. Tan, Y. Li, C. Yu, T. Zhai, Y. Bando, S. Yang and B. Zou, Adv. Funct. Mater. **22**, 2081 (2012).

[14] V. I. Klimov, S. Hunsche, and H. Kurz, Phys. Rev. B **50**, 8110 (1994).

[15] Semiconductor and Metal Nanocrystals: Synthesis and Electronic and Optical Properties, ed. by V. I. Klimov, Dekker, New York, (2004).

[16] The pump fluence (j_p) is presented in terms of the number of photons per cm^2.

[17] J. Nanda, S. A. Ivanov, H. Htoon, I. Bezel, A. Piryatinski, S. Tretiak, and V. I. Klimov, J. Appl. Phys. **99**, 034309 (2006).

[18] K. Dohnalová, A. N. Poddubny; A. A. Prokofiev, A. M. W. D. de Boer; C. P. Umesh; J. M. J. Paulusse, H. Zuilhof, and T. Gregorkiewicz, Light: Sci. Appl. **2**, e47 (2013).

[19] J. H. Sun, J. L. Zhao, and Y. Masumoto, Appl. Phys. Lett. **102**, 053119 (2013).

[20] S. L. Sewall, R. R. Cooney, K. E. H. Anderson, E. A. Dias, D. M. Sagar, and P. Kambhampati, J. Chem. Phys. **129**, 084701 (2008).
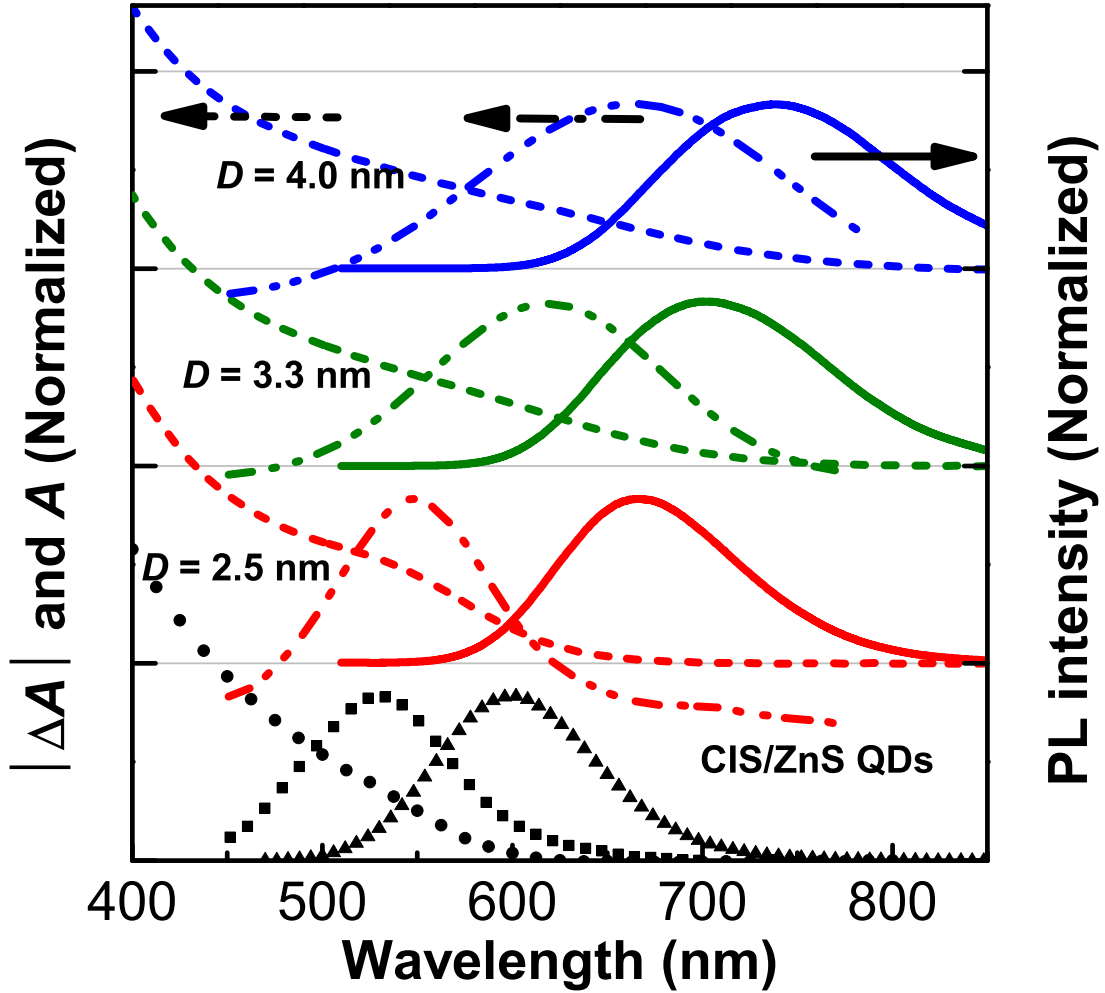
FIG. 3.2 Steady-state absorption (A) (dashed lines), photoluminescence (PL) spectra (solid lines) and TA spectra (dash-dotted lines) of $CuInS_2$ QDs with three average diameters. Steady-state absorption (circles), PL spectra (triangles) and TA spectra (squares) of $CuInS_2$/ZnS core/shell QDs with core diameters of 2.5 nm. By the peak values ΔA and PL normalized. The absorption is normalized at 450 nm. For TA measurement, the pump fluence is set to $\langle N_0 \rangle = 0.5$ for each sample (average number of absorbed photons equals to 0.5) at wavelength of 400 nm and pump-probe delay time is 4 ps.
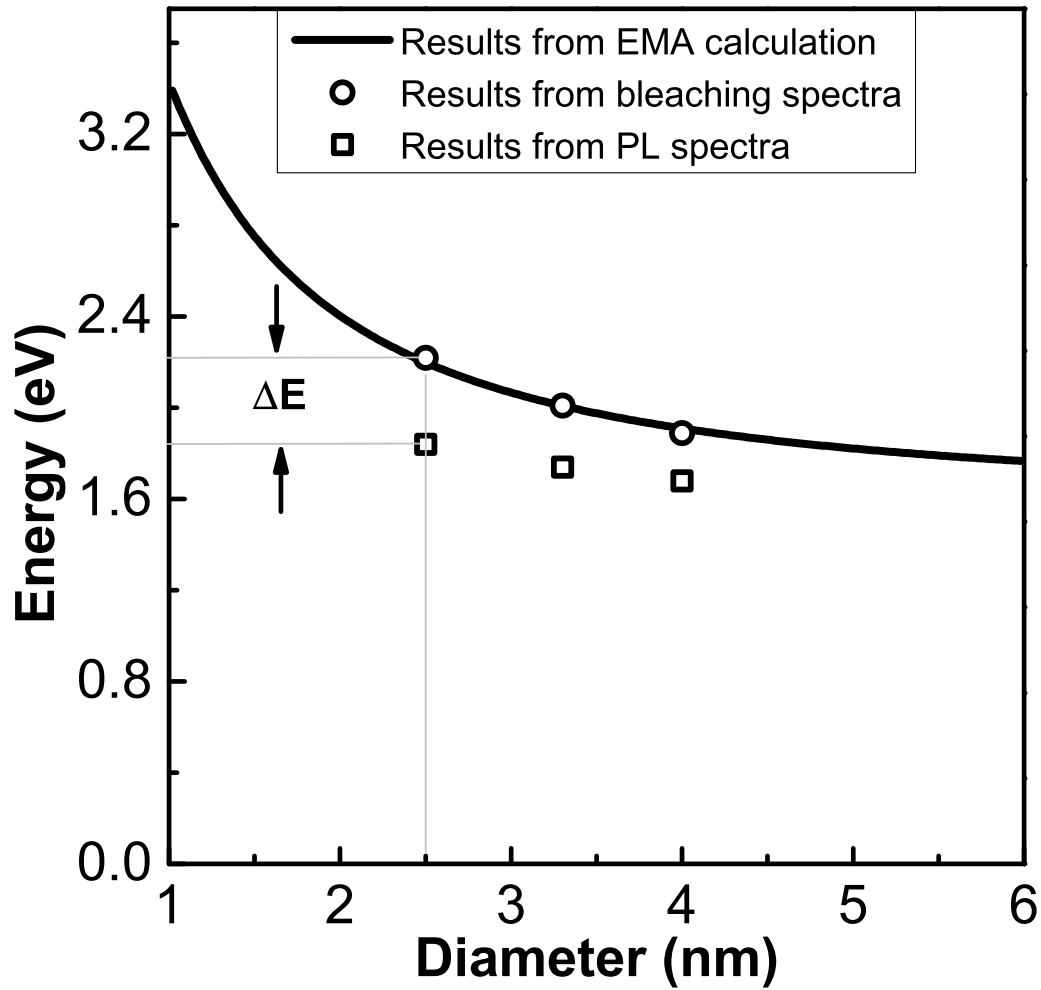
FIG. 3.3 The size-dependent 1S transitions determined from bleaching spectra is illustrated by circles and size-dependent energy levels of PL are illustrated by squares. The solid line represents the calculated band gaps as a function of the diameters of $CuInS_2$ QDs on the finite-depth-well model in the effective mass approximation (EMA).
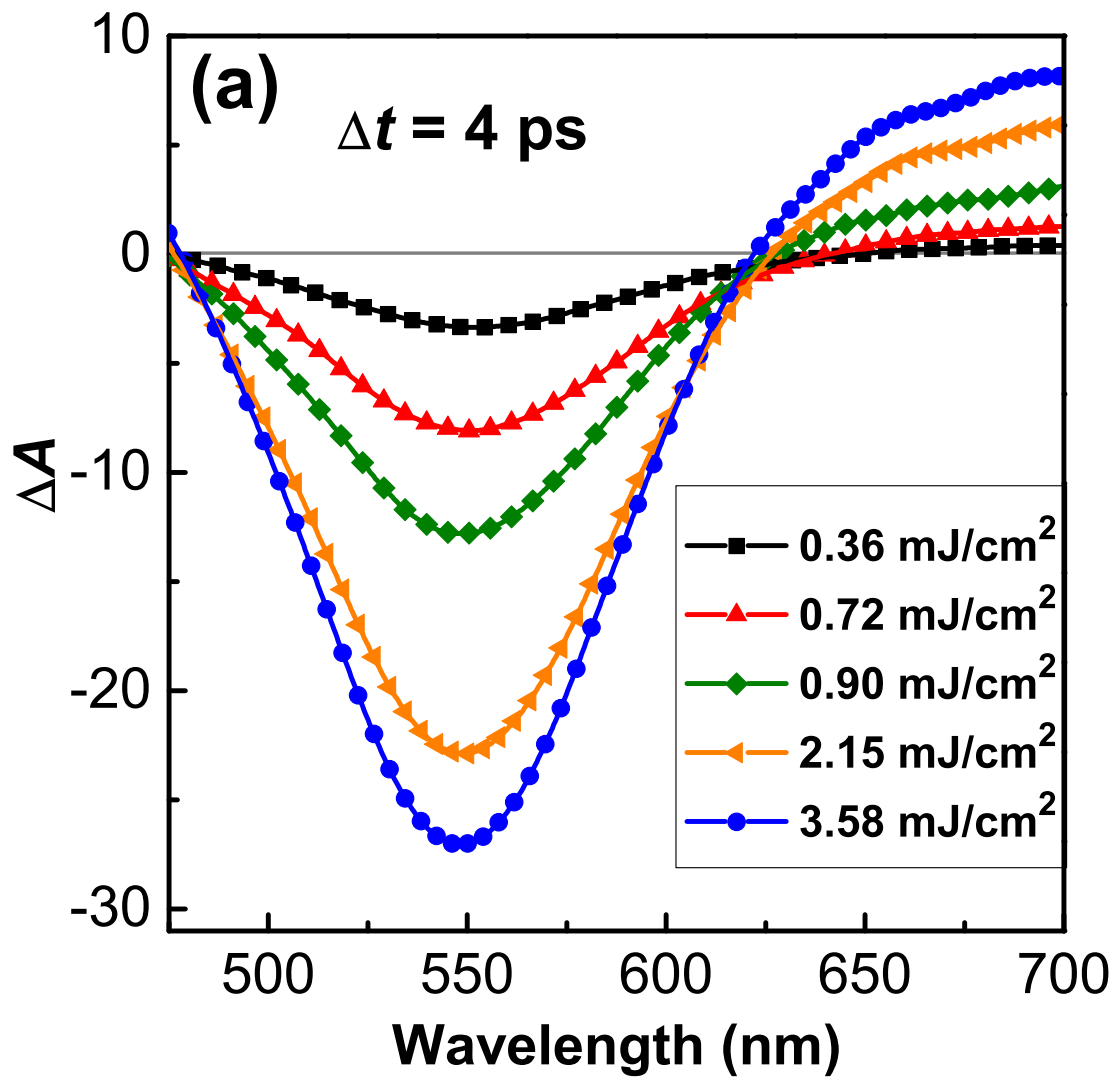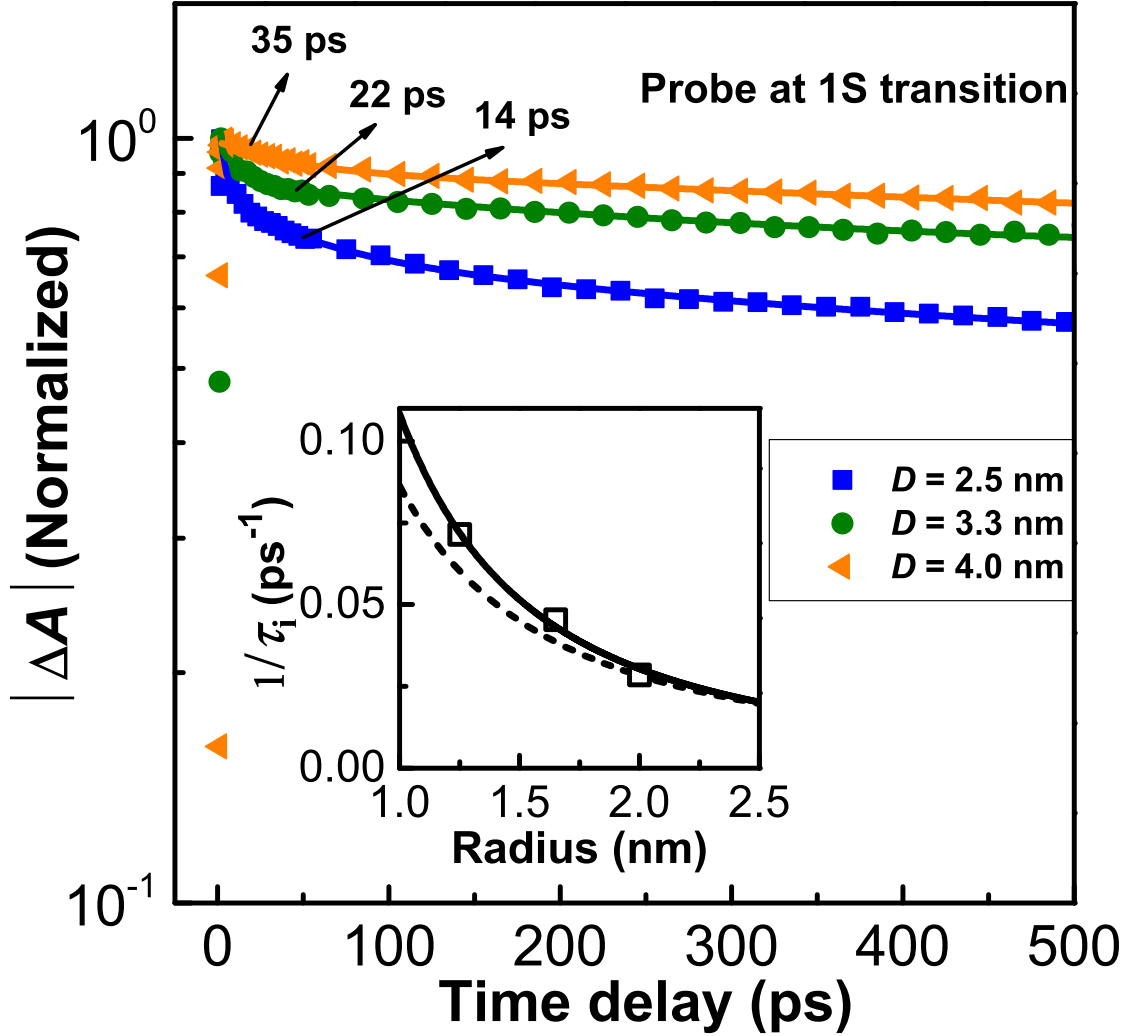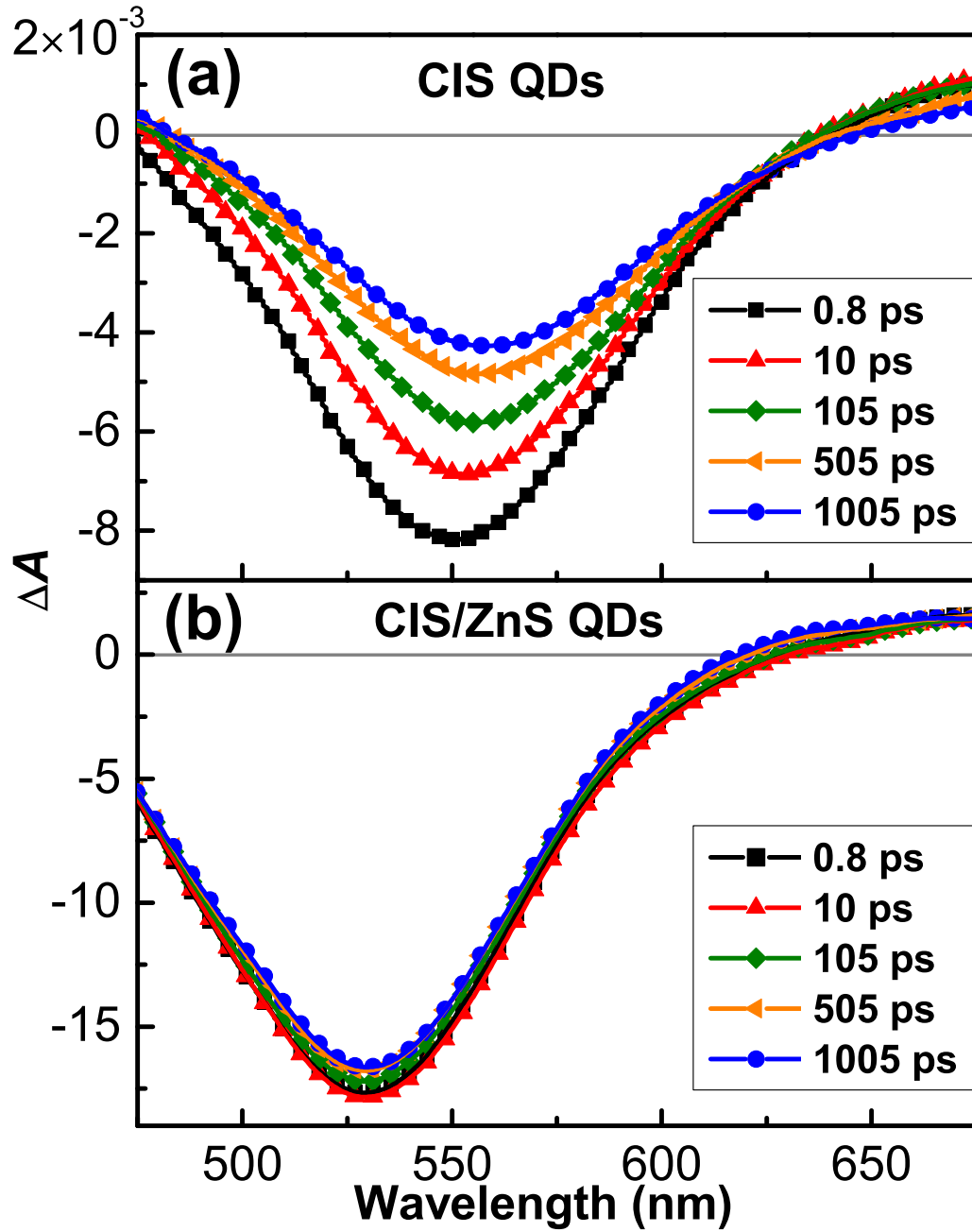
FIG. 3.4 Transient absorption spectra of CuInS$_2$ QDs 2.5 nm in diameter recorded at five pump fluencies.
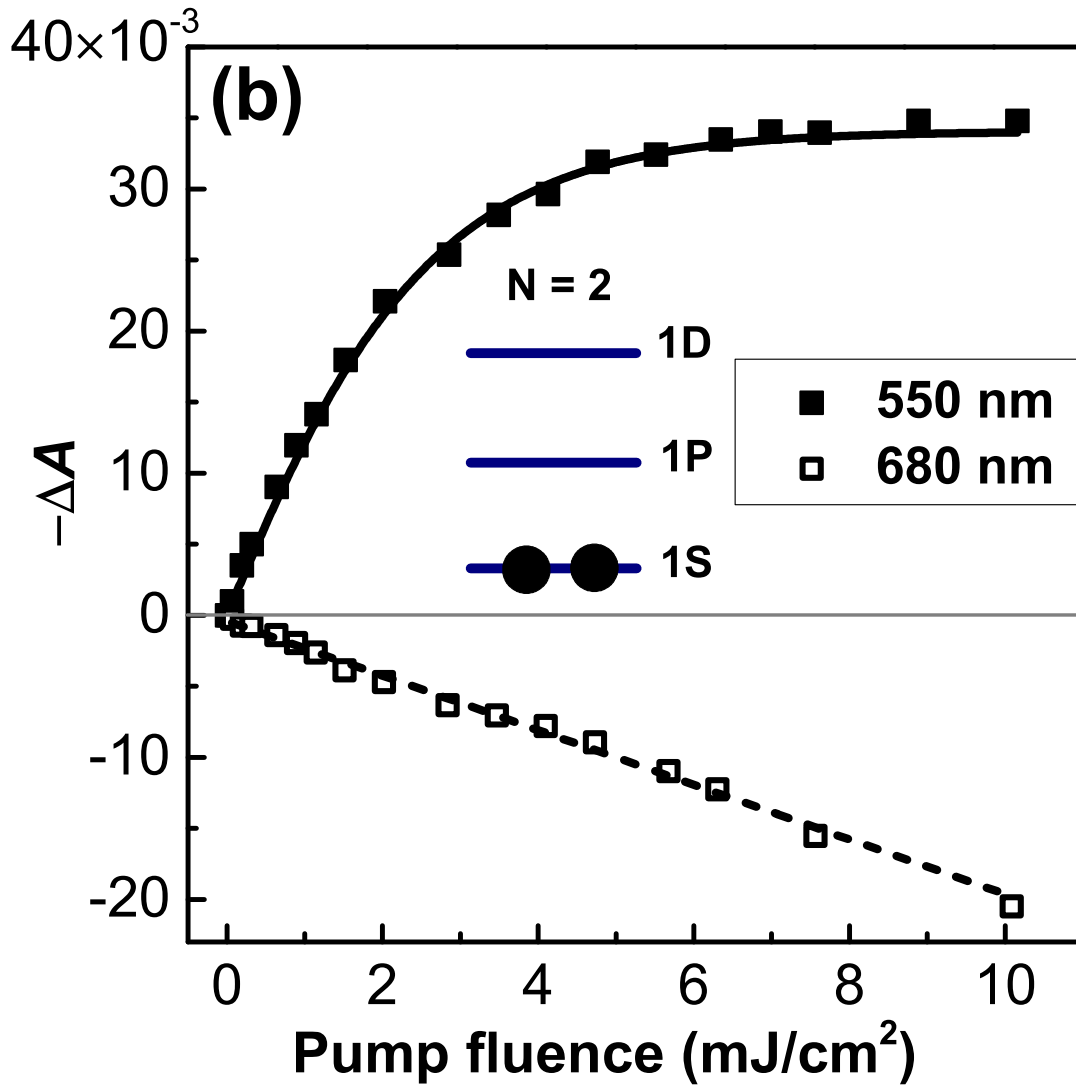
FIG. 3.5 The bleach amplitude of $CuInS_2$ QDs at the 1S absorption peak as a function of the pump fluence. Pump-probe delay time is 4 ps and the solid line is the best fit by Eq. (3.1) in the text.

FIG. 3.6 The normalized TA kinetics of CuInS$_2$ QDs with three diameters. The rates of the electron trapping are plotted in the inset by hollow squares. The solid line in the inset shows the fit by a power-law expression. The calculated electron densities at the QD surface as a function of radius are shown by a dashed line in the inset. The electron densities were normalized to the slowest measured-trapping-rate for comparison. For TA measurement, the pump fluence is set to $\langle N_0 \rangle = 0.5$ for each sample (average number of absorbed photons equals to 0.5) at wavelength of 400 nm.

FIG. 3.7 Transient absorption spectra of (a) CuInS$_2$ QDs and (b) CuInS$_2$/ZnS QDs in toluene. The pump fluence is set to $\langle N_0 \rangle = 0.5$ for each sample (average number of absorbed photons equals to 0.5) at wavelength of 400 nm.
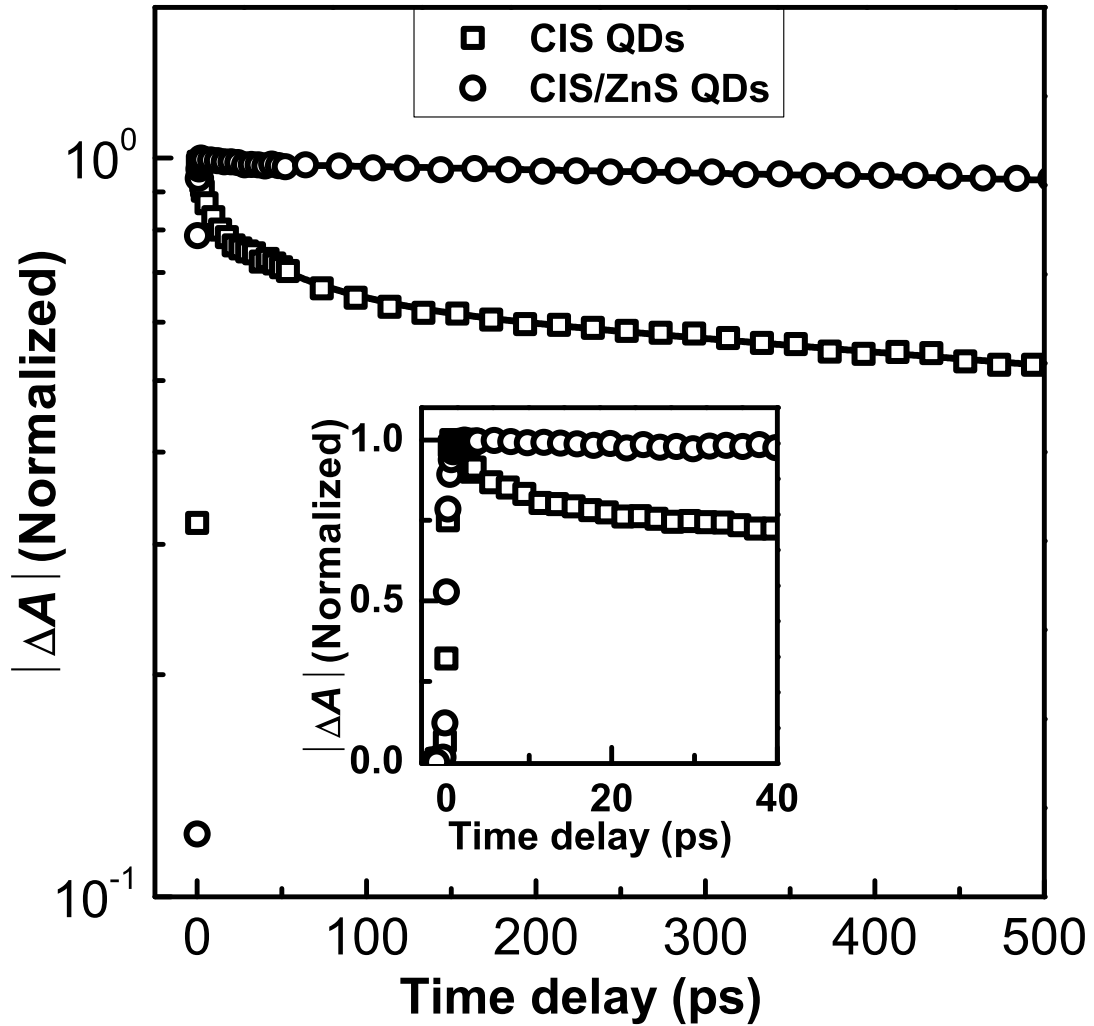
FIG. 3.8 The normalized TA kinetics of $CuInS_2$ QDs and $CuInS_2/ZnS$ core/shell QDs. The inset shows the enlarged TA kinetics in a short time scale. The probe wavelengths for $CuInS_2$ and $CuInS_2/ZnS$ core/shell QDs are 550 and 530 nm, respectively. For TA measurement, the pump fluence is set to $\langle N_0 \rangle = 0.5$ for each sample (average number of absorbed photons equals to 0.5) at wavelength of 400 nm.

Chapter 4

Electron transfer from CuInS$_2$ quantum dots to TiO$_2$ films

4.1 Introduction

Quantum dots (QDs) have been considered as a revolutionizing material in next-generation photovoltaics (PVs)[1,2] because of their size-dependent properties, flexible solution-processing, and higher photostability compared to traditional organic dyes. Efficient electron transfer (ET) from QDs to external electrodes is a key factor to achieve high power-conversion-efficiency in PVs. From Marcus theory,[3] the ET rate is determined by the electronic coupling strength (H_{DA}), the total reorganization energy (λ), and the driving force energy (ΔG). In donor-acceptor hybrid systems of CdSe,[4–6] CdS[7] and PbS QDs[8] tethered to TiO$_2$ or ZnO, the effects of above three parameters on the ET dynamics have been explored widely. The photoelectrochemical response has been tuned via the size control of CdSe QDs to obtain the maximum photoconversion efficiency in QD-sensitized solar cells.[6] It is well known that overcoating CdSe QDs with wide band-gap shell materials, such as ZnS, to form type I core/shell structures can greatly

enhance their photo- and thermal-stability[9] and efficiency[10] in QD-sensitized solar cells. Bulk $CuInS_2$ has a direct bandgap of 1.53 eV, which is well matched with the optimal spectral range for photovoltaic applications, resulting in Cd-free solar harvesters in solar cells. The band gap of $CuInS_2$ QDs can be tuned not only by controlling their size[11, 12] and stoichiometry[13, 14], but also by introducing other elements such as Zn[15–18]. Therefore, they are considered to be alternative low-toxicity materials as solar harvesters for the solution-processed PVs.[19] We need to fully understand the extraction efficiency of photogenerated charges from $CuInS_2$ QDs to the external electrodes, such as TiO_2, by controlling their size and surface structures for better performances of the PVs.

In this chapter, we demonstrated efficient electron injection from $CuInS_2$ core and $CuInS_2$/ZnS core/shell QDs to the porous anatase TiO_2 films by using steady-state and time-resolved photoluminescence (PL) spectroscopy. The relevant energy levels of $CuInS_2$ QDs are obtained by cyclic voltammetry (CV) measurements, which is in accordance with the values calculated by the effective mass approximation (EMA).[12] The lowest unoccupied molecular orbital (LUMO) level in $CuInS_2$ QDs is above that of the TiO_2 films, resulting in the efficient electron injection into TiO_2 films from $CuInS_2$ QDs. The effect of the core diameter and the ZnS shell thickness on the ET rate and efficiency is studied in detail. We make the tunneling calculation to describe the ET rate as a function of the shell thickness and to understand the ET rate and efficiency in the QD/TiO_2 system.

4.2 Experimental

4.2.1 Sample preparation

The $CuInS_2$ core and $CuInS_2$/ZnS core/shell QDs were synthesized by means of the wet chemical method.[13] Transmission electron microscopy (TEM) images of the QDs are shown in the inset of Fig. 2.5, which determine the diameters of three samples of
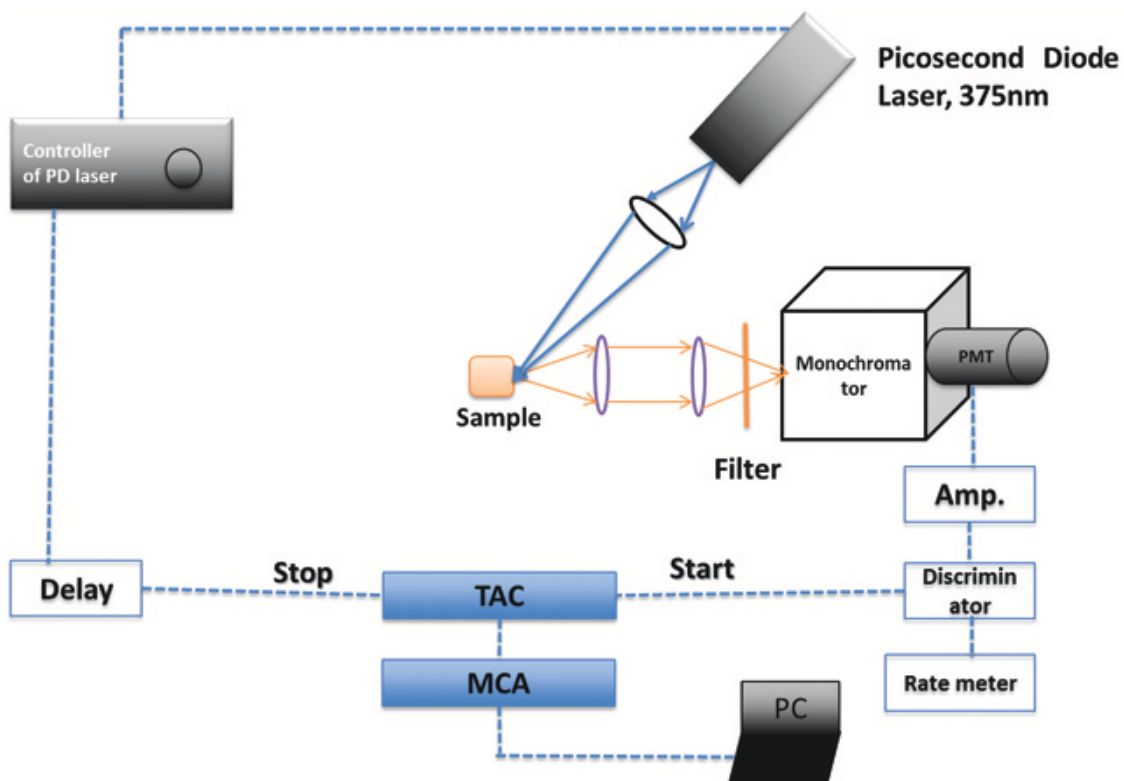
FIG. 4.1 Optical setup of the time-correlated single photon counting system.

CuInS$_2$ core QDs to be 2.5, 3.3, and 4.0 nm, respectively. Furthermore, the CuInS$_2$ core QDs were coated with a ZnS shell to form the CuInS$_2$/ZnS core/shell QDs by means of a successive ionic layer adsorption and reaction (SILAR) methods.[13] The size and the size distribution histogram of the CuInS$_2$/ZnS core/shell QDs determined by TEM are shown in Fig. 2.6. The TiO$_2$ and ZrO$_2$ metallic oxide electrodes used in this work were fabricated by the same method reported by Heimer et al.[20] As for the QDs-sensitization, metallic oxide electrodes were tethered 3-mercaptopropionic acid (MPA) first and then immersed in QDs in toluene.[6]

4.2.2 Time-correlated single photon counting system

Time-resolved PL was measured by means of a time-correlated single photon counting (TCSPC) system with a visible photomultiplier and a 70 ps picosecond pulsed diode laser emitting at 375 nm. Time resolution of the TCSPC system was about 1 ns.

4.3 Experimental results and discussion

4.3.1 Energy levels of CuInS$_2$ quantum dots

The absorption and PL spectra of synthesized CuInS$_2$ core QDs are shown in Fig. 4.2. The absorption edge gradually shifts toward longer wavelength with increasing the diameter of the QDs, in consistent with quantum confinement effect. Emission peaks of the QDs exhibit a large Stokes shift of about 300 meV from their corresponding optical band gaps, indicating that the radiative transition does not come from excitonic recombination.[11–14]

The LUMO and the highest occupied molecular orbital (HOMO) energy levels of the CuInS$_2$ core QDs were obtained from a CV method. The resulting energy levels shown in Fig. 4.3 by red circles are consistent with the energy levels calculated in EMA with a finite-depth well,[12] where LUMO and HOMO levels of bulk CuInS$_2$ are assumed to be -4.1 eV and -5.6 eV,[21] respectively. The effective masses of electrons and holes are $0.16m_0$ and $1.30m_0$, respectively, where the m_0 is the electron mass in vacuum.[10] The LUMO level of the porous anatase TiO$_2$ film obtained from the CV method is located at -4.21 eV, which is much lower than the LUMO level of -3.88 eV for the largest CuInS$_2$ core QDs. Therefore, the ET from the QDs to the porous anatase TiO$_2$ films is energetically allowable. According to the Marcus theory, the ET between two states is dominated by ΔG.[3,4] In the case of electron injection into TiO$_2$, the ΔG is the difference between the lowest quantum electron level of the QDs and the LUMO level of TiO$_2$. As the

Table 4.1 The efficiency (η_{ET}) and the rate (κ_{ET}) of electron transfer (ET) from CuInS$_2$ QDs to the porous anatase TiO$_2$ film.

Diameters of CuInS$_2$ QDs (nm)	κ_{ET} (10^7s^{-1})	η_{ET} (%)
2.5	6.0	69
3.3	5.4	74
4.0	4.5	83

ΔG between acceptor and donor systems increases, the ET rate increases and reaches a maximum when the ΔG is equal to the reorganization energy.

4.3.2 Electron transfer from CuInS$_2$ quantum dots to TiO$_2$ films

In Fig. 4.4, PL decay curves of the CuInS$_2$ core QDs 2.5, 3.3, and 4.0 nm in average diameter deposited on TiO$_2$ and ZrO$_2$ films are shown. From the PL dynamics of the CuInS$_2$ core QDs, the fast decay comes from nonradiative surface-traps and the slow decay comes from radiative recombination emission. Recently, the long lifetime emission was suggested to originate from the recombination from an electron quantum state to a localized hole state.[11] The LUMO level of the ZrO$_2$ film was obtained to be -3.17 eV, which is even higher than the LUMO level of -3.65 eV in the smallest CuInS$_2$ core QDs. Therefore, the ET from CuInS$_2$ QDs to ZrO$_2$ is energetically unfavorable, and thus the observed PL decay curves in this system can be used as a reference. The significant shortening in the PL decays of CuInS$_2$ core QDs is clearly observed. This suggests that the ET adds another decay channel to the excited states of the QDs. To calculate the ET rate, we assume that the average PL lifetimes of the QDs on TiO$_2$ and ZrO$_2$ films are given by $\tau_{\text{QD}-\text{TiO}_2} = 1/(k_{\text{R}} + k_{\text{NR}} + k_{\text{ET}})$ and $\tau_{\text{QD}-\text{ZrO}_2} = 1/(k_{\text{R}} + k_{\text{NR}})$, respectively, where k_{R} and k_{NR} are radiative and nonradiative decay rates for QDs, respectively.[4–6] The ET rate (k_{ET}) and efficiency (η_{ET}) can be calculated as: $k_{\text{ET}} = 1/\tau_{\text{QD}-\text{TiO}_2} - 1/\tau_{\text{QD}-\text{ZrO}_2}$ and $\eta_{\text{ET}} = 1 - \tau_{\text{QD}-\text{TiO}_2}/\tau_{\text{QD}-\text{ZrO}_2}$, respectively. The evaluated ET rates and efficiencies are

summarized in Table 1. The ET rate reaches 10^7 s^{-1} close to the rate in CdSe-TiO$_2$ donor-acceptor systems.[4,6,23] The rate slightly increases with decreasing the core diameters of the CuInS$_2$ QDs, in consistent with the Marcus theory. However, the size dependence of the ET rate is clearly lower than that of CdSe QDs.[4] On the other hand, the ET efficiency shows the opposite trend. The maximum efficiency is obtained in the largest CuInS$_2$ QDs. It has been reported the ET process is impeded in QDs by the considerable amount of surface-localized trap states.[1,5] Considering that the luminescence of the CuInS$_2$ QDs is significantly reduced by the surface traps and that the PL lifetimes of CuInS$_2$ QDs in toluene are shortened with decreasing the diameters, we attribute the low ET efficiency in small CuInS$_2$ QDs to the relatively large amount of surface-localized states.

As is known, the stability of bare QDs remains an issue due to photo-induced oxidation in photovoltaic devices.[5] We further investigated photoinduced ET into TiO$_2$ from CuInS$_2$/ZnS core/shell QDs. With increasing the ZnS shell thickness, the PL peak of the QDs slightly shifts to higher energy compared with the bare QDs, which is slightly different from the case of CdSe/ZnS core/shell QDs.[11,13] For CuInS$_2$/ZnS core/shell QDs, the surface coating by a ZnS shell involves an interdiffusion alloying process, perhaps resulting in formation of an inner alloying layer and etching of the CuInS$_2$ cores. However, we ignored the size change of the CuInS$_2$ core in order to facilitate the estimation of the ZnS shell thickness. As shown in Fig. 4.5, the PL lifetimes of the CuInS$_2$/ZnS core/shell QDs tethered onto the ZrO$_2$ films exhibit a significant increase with increasing the shell thickness, suggesting the improved passivation of surface defects in the QDs.

In Fig. 4.5, PL decay curves of the two series of CuInS$_2$/ZnS core/shell QDs 2.5 and 4.0 nm in core diameter tethered onto the TiO$_2$ films are shown. It is expected that the ZnS shell acts as a tunneling barrier for ET from the photoexited CuInS$_2$ QDs to the TiO$_2$ film because the H_{DA} between CuInS$_2$ QDs and a TiO$_2$ film would be weakened with increasing the ZnS shell thickness. The ET rates for the two series of core/shell QDs

plotted as a function of ZnS shell thickness are shown in Fig. 4.6. As we expected, the ET rate rapidly decreases with increasing the ZnS shell thickness. The decrease in the ET rate is considered to result from the weak electronic coupling between the TiO_2 films and the QDs with the increase of the ZnS shell thickness. Surprisingly, the ET efficiency slightly decreases with the increase of ZnS shell thickness. For example, the ET efficiency of QDs 2.5 nm in core diameter decreases from 65% for the 1.1 monolayer (ML) ZnS shell to 38% for the 3.2 ML ZnS shell. Despite the significant decrease in the ET rate in contrast with that for the $CuInS_2$ core QDs, the $CuInS_2$/ZnS core/shell QDs exhibit only a slight reduction in ET efficiency with increasing the ZnS shell thickness. This is because a thin ZnS shell can effectively reduce the number of the traps as nonradiative recombination centers and results in efficient enhancement in the PL quantum efficiency.[11] This gives us a hint that how we can control the ET rate and the ET efficiency in such a donor-accepter system by controlling the QDs shell thickness to optimize the performance of the QD-based solar cells.

4.3.3 Electron tunneling model

We assume the LUMO and HOMO levels of the $CuInS_2$ core remain unchanged for different thickness of the ZnS shell and ignore the intersphere distance between the $CuInS_2$/ZnS QDs and TiO_2 films.[23] The ET rates should be related to the thickness of the shell and could be described by the following expression:[5, 22]

$$k(d) = k_0 \mathrm{e}^{-\beta d} \, , \tag{4.1}$$

where d is the thickness of the ZnS shell, k_0 is the ET rate for bare QDs. Experimental plots of the two series of ET rates as a function of ZnS shell thickness can be well fitted by the above equation. The good fit confirms the tunneling of the electron through the ZnS

barrier shell. The fitting by the equation (4.1) yields semilogarithmic slopes, β, of 1.1 and 1.4 nm^{-1} for $CuInS_2$/ZnS core/shell QDs 2.5 and 4.0 nm in core diameter, respectively. The slope is comparable to reported one (3.5 nm^{-1}) for CdSe QDs.[5] The value of β for 2.5 nm QDs is less than that in the 4.0 nm QDs. This is because β is dependent on the barrier height for the $1S$ electron in the $CuInS_2$ core to tunnel into the ZnS shell. Therefore, the $1S$ electron in the small $CuInS_2$ core is easier to tunnel into the ZnS shell than that in the large core, resulting in smaller factor β.

The eigen function and energy of the electron in $CuInS_2$/ZnS core/shell QDs were calculated to quantify the effect of ZnS shell thickness on the ET rate by modeling them as a particle confined in a spherical well of finite depth.[24, 25] The effective mass of electrons is $0.28m_0$ for ZnS.[5] The LUMO levels are -4.1 eV for the $CuInS_2$ core, -3.1 eV for the ZnS shell[5] and -0.4 eV for the MPA, as shown in Fig. 4.7.[26] To intuitively illustrate the radial distribution of the wave function for the 1S electron, we performed a potential well calculation in spherical symmetry for $CuInS_2$/ZnS core/shell QDs with a 4 ML ZnS shell, as shown in Fig. 4.7. The electron wave functions spread into the ZnS shell and their amplitudes decrease exponentially with increasing the shell thickness. We performed the calculation for the $CuInS_2$/ZnS core/shell QDs having the same core and ZnS shells differently thick. The diameter of the $CuInS_2$ core was chosen to be 2.5 and 4.0 nm based on TEM images. As shown in Fig. 4.6, the calculated radial electron densities at the ZnS surface as a function of the ZnS shell thickness are in reasonable agreement with the experimental plots of the shell-thickness-dependent ET rates for the two series of $CuInS_2$/ZnS core/shell QDs. The good agreement with the theoretical calculation confirms the tunneling of the electron through the ZnS barrier shell. On the other hand, this result suggests that optimizing ET efficiency can be realized by controlling the density of the surface states and the ET rate via the change of the shell thickness.

4.4 Conclusions

In summary, we have investigated the ET process from $CuInS_2$ core and $CuInS_2$/ZnS core/shell QDs to the porous anatase TiO_2 film. The ET rate reaches 10^7 s^{-1} for different-sized $CuInS_2$ core QDs. The ET rate as a function of shell thickness was well expressed by an exponential function for the core/shell QDs with core diameters of 2.5 nm and 4.0 nm. This trend is well explained by the electron tunneling calculation of the core/shell QDs. The ET rate is proportional to the existing probability of electrons at the QD surface decreasing exponentially with increasing the shell thickness. These results show the possible ways of optimizing the ET efficiency and QD stability by controlling the core size and shell thickness in QD-based solar cells.

Bibliography

[1] W. U. Huynh, J. J. Dittmer, and A. P. Alivisatos, Science **295**, 2425 (2002).

[2] I. Gur, N. A. Fromer, M. L. Geier, and A. P. Alivisatos, Science **310**, 462 (2005).

[3] R. A. Marcus, J. Chem. Phys. **24**, 966 (1956).

[4] K. Tvrdya, P. A. Frantsuzovc, and P. V. Kamat, Proc. Natl. Acad. Sci. **108**, 29 (2011).

[5] H. Zhu, N. Song, and T. Lian, J. Am. Chem. Soc. **132**, 15038 (2010).

[6] A. Kongkanand, K. Tvrdy, K. Takechi, M. Kuno, and P. V. Kamat, J. Am.Chem. Soc. **130**, 4007 (2008).

[7] D. F, Waton, J. Phys. Chem. Lett. **1**, 2299 (2010).

[8] B. R. Hyun, A. C. Bartnik, J. K. Lee, H. Imoto, L. Sun, J. J. Choi, Y. Chujo, T. Hanrath, C. K. Ober, and F. W. Wise, Nano Lett. **10**, 31 (2010).

[9] J. B. Sambur and B. A Parkinson, J. Am. Chem. Soc. **132**, 2130 (2010).

[10] Q. Shen, J. Kobayashi, L. J. Diguna, and T. Toyoda, J. Appl. Phys. **103**, 084304 (2008).

[11] L. Li, A. Pandey, D. J. Werder, B. P. Khanal, J. M. Pietryga, and V. I. Klimov, J. Am. Chem. Soc. **133**, 1176 (2011).

[12] H. Zhong, S. S. Lo, T. Mirkovic, Y. Li, Y. Ding, Y. Li, and G. D. Scholes, ACS Nano. **4**, 5253 (2010).

[13] W. S. Song and H. Yang, Appl. Phys. Lett. **100**, 183104 (2012).

[14] B. Chen, H. Zhong, W. Zhang, Z. Tan, Y. Li, C. Yu, T. Zhai, Y. Bando, S. Yang, and B. Zou, Adv. Funct. Mater. **22**, 2081 (2012).

[15] J. Zhang, R. Xie, and W. Yang, Chem. Mater. **23**, 3357 (2011).

[16] W. Zhang and X. Zhong, Inorg. Chem. **50**, 4065 (2011).

[17] X. Tang, W. Cheng, E. S. G. Choo, and J. Xue, Chem. Commun. **47**, 5217 (2011).

[18] X. Yuan, J. L. Zhao, P. T. Jing, W. J. Zhang, H. B. Li, L. G. Zhang, X. H. Zhong, and Y. Masumoto, J. Phys. Chem. C. **116**, 11973 (2012).

[19] E. Arici, N. S. Sariciftci, and D. Meissner, Adv. Funct. Mater. **13**, 165 (2003).

[20] T. A. Heimer, S. T. D'Arcangelis, F. Farzad, J. M. Stipkala, and G. J. Meyer, Inorg. Chem. **35**, 5319 (1996).

[21] All the energy levels in this chapter are relative to the vacuum level.

[22] Z. Xu, C. R. Hine, M. M. Maye, Q. Meng, and M. Cotlet, ACS Nano. **4**, 3357 (2011).

[23] K. Tvrdy and P. V. Kamat, J. Phys. Chem. A. **113**, 3765 (2009).

[24] J.W. Haus, H. S. Zhou, I. Honma, and H. Komiyama, Phys. Rev. B **47**, 1359 (1993).

[25] D. Schooss, A. Mews, A. Eychmüller, and H. Weller, Phys. Rev. B **49**, 17072 (1994).

[26] Z. Ning, M. Molnár, Y. Chen, P. Friberg, L. Gan, H. Ågren, and Y. Fu, Phys. Chem. Chem. Phys. **13**, 5848 (2011).
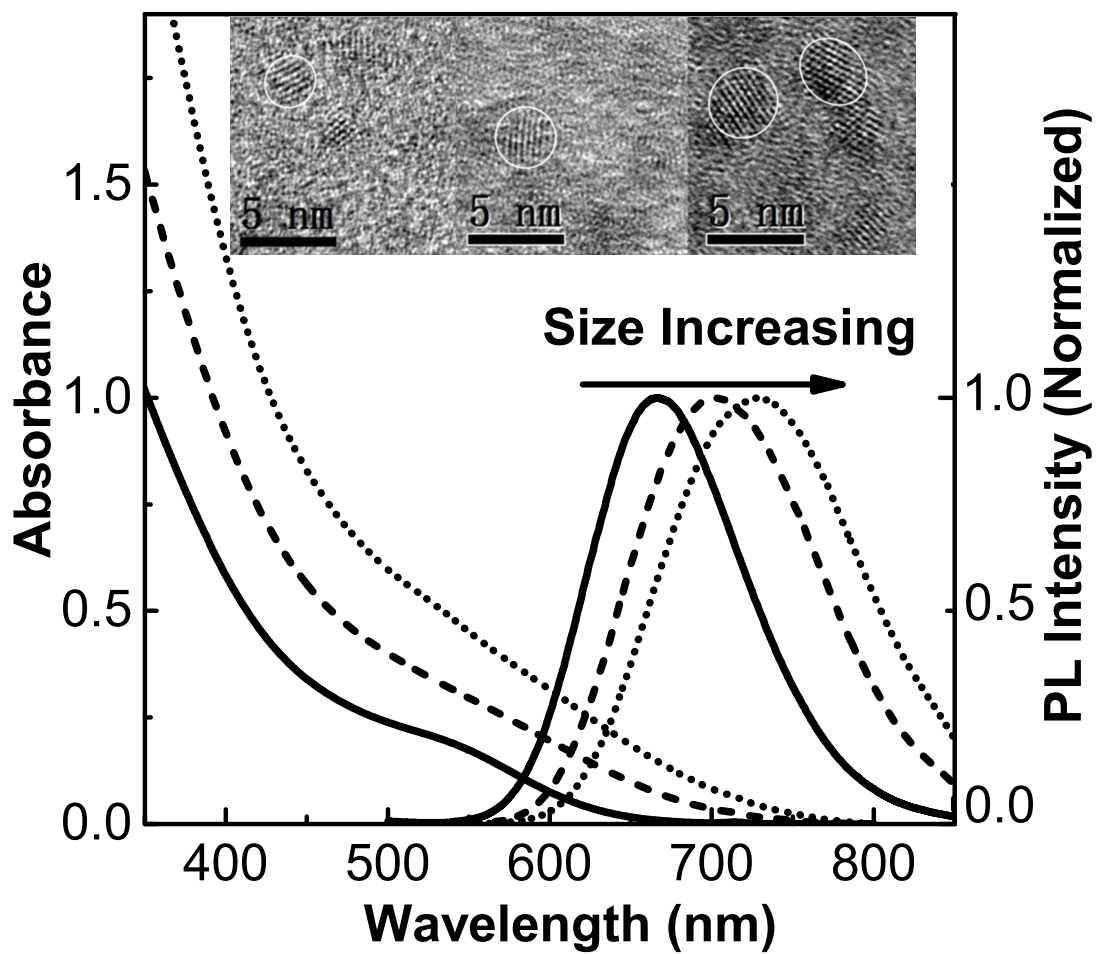
FIG. 4.2 Steady-state photoluminescence (PL) and absorption spectra of CuInS$_2$ core QDs with diameters of 2.5nm, 3.3nm, and 4.0 nm, respectively, in toluene and the corresponding high-resolution TEM image from left to right. The scale bar is 5 nm.
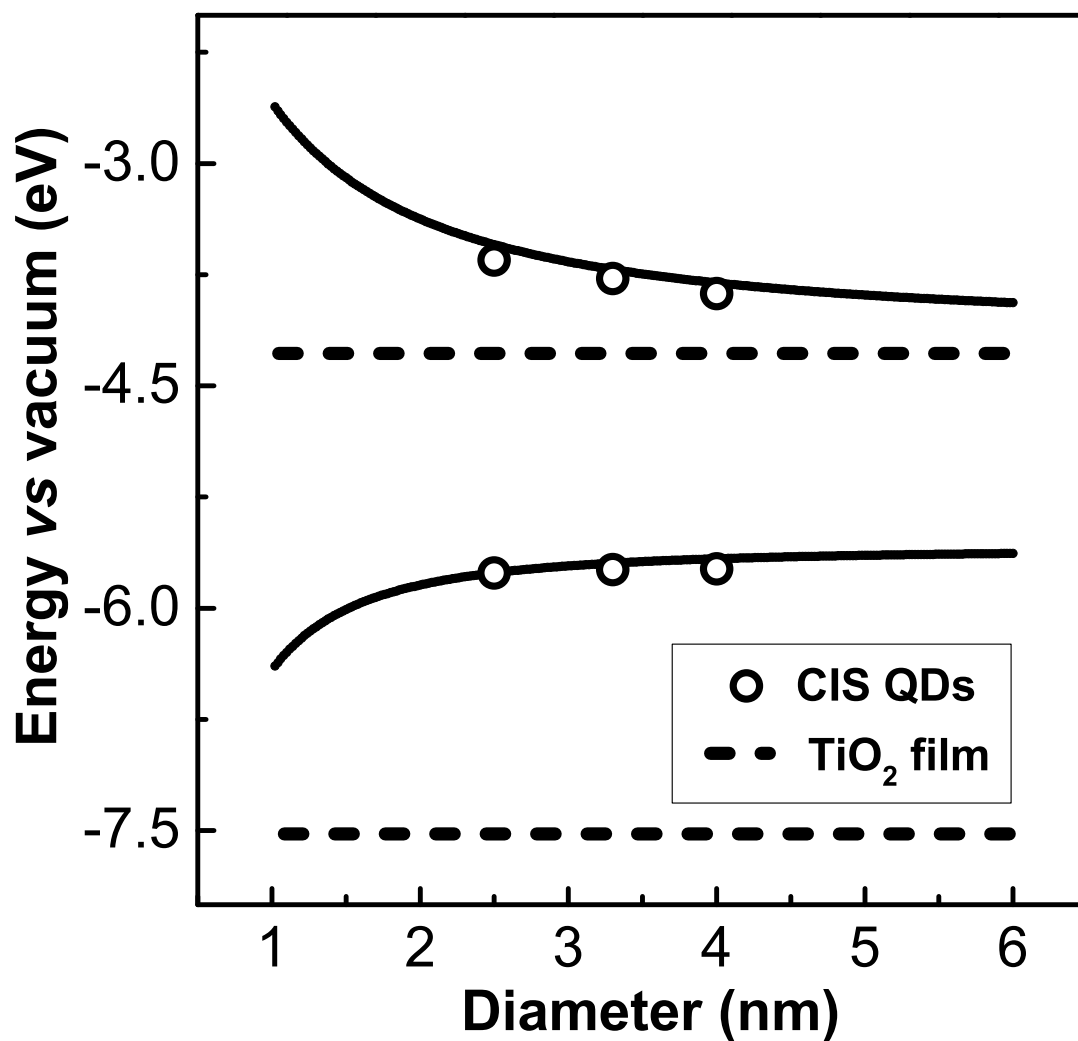
FIG. 4.3 The lowest unoccupied molecular orbital (LUMO) and highest occupied molecular orbital (HOMO) levels of $CuInS_2$ QDs shown by circles were measured by cyclic voltammetry (CV). Solid lines represent LUMO and HOMO levels of the $CuInS_2$ QDs calculated in effective mass approximation (EMA). Dashed lines represent the LUMO and HOMO levels of the TiO_2 film measured by CV and optical absorption.
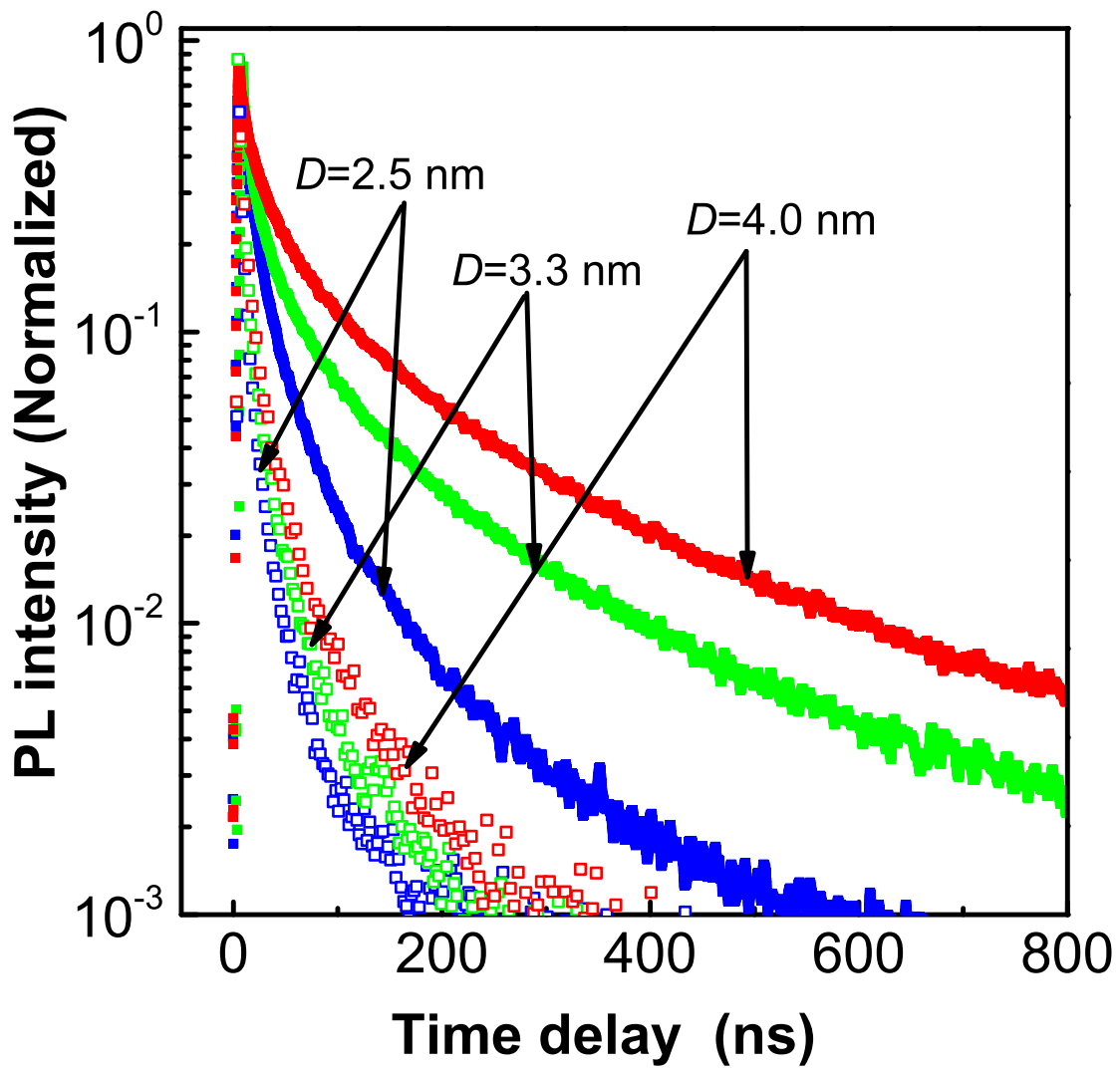
FIG. 4.4 Photoluminescence decay curves of CuInS$_2$ core QDs deposited on the ZrO$_2$ (solid masks) and TiO$_2$ films (open masks).
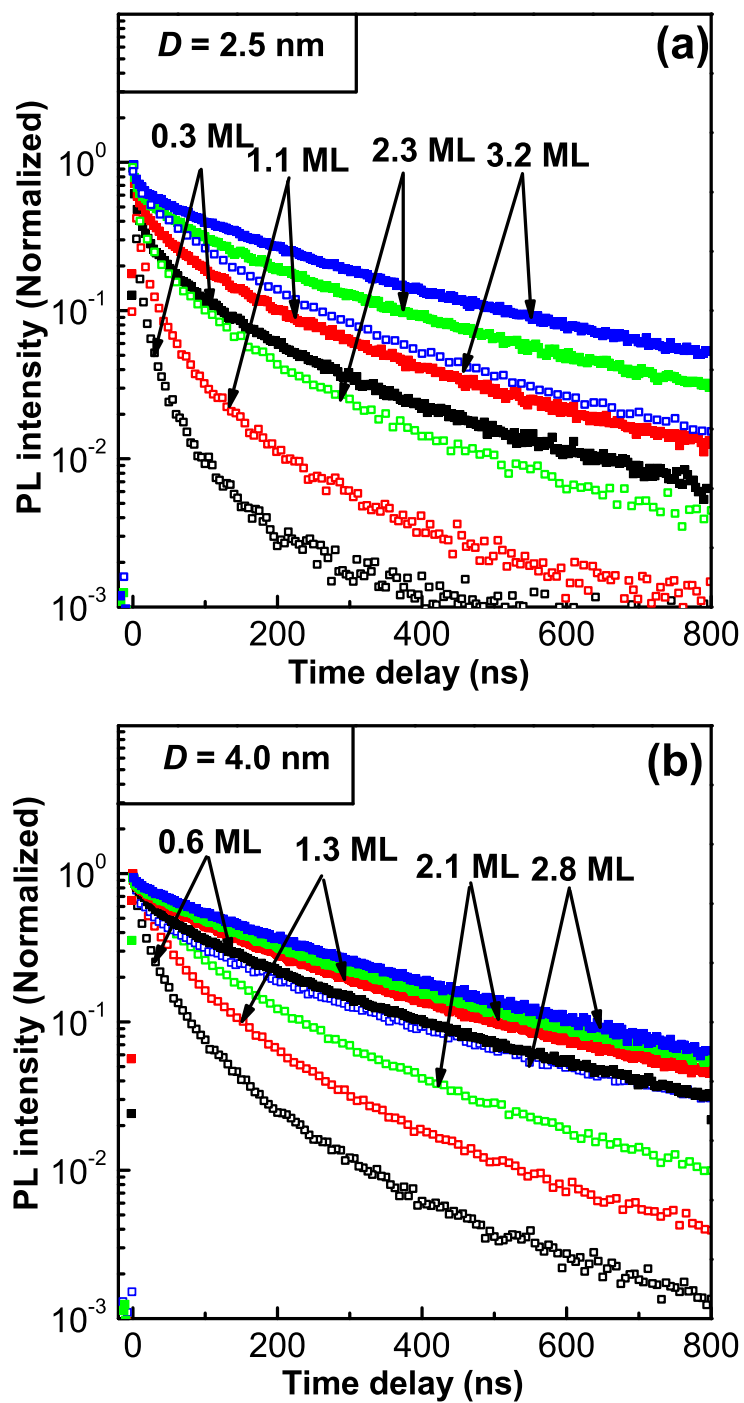
FIG. 4.5 Photoluminescence decay curves of CuInS$_2$/ZnS core/shell QDs with various core diameters and the ZnS shell thicknesses deposited on the ZrO$_2$ (solid masks) and TiO$_2$ films (open masks).
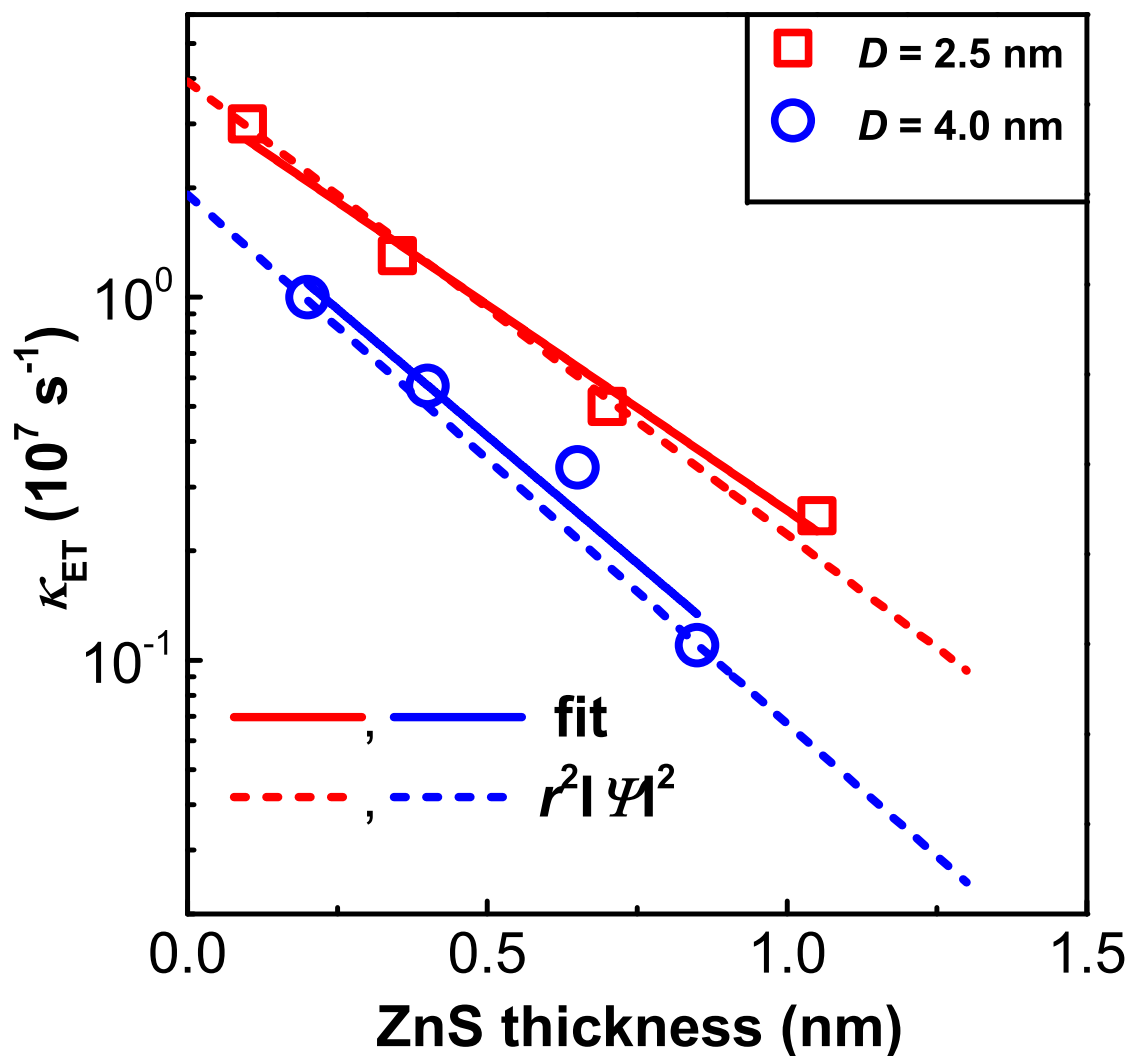
FIG. 4.6 Plots of electron transfer (ET) rates of CuInS$_2$/ZnS core QDs with core diameters of D=2.5 nm (squares) and D=4.0 nm (circles), respectively, as a function of ZnS shell thickness. The solid line represents the fit of the ET rate. The calculated electron densities at the ZnS surface as a function of ZnS shell thickness are shown by dashed lines. The electron densities were normalized to the fastest measured ET rates for comparison.
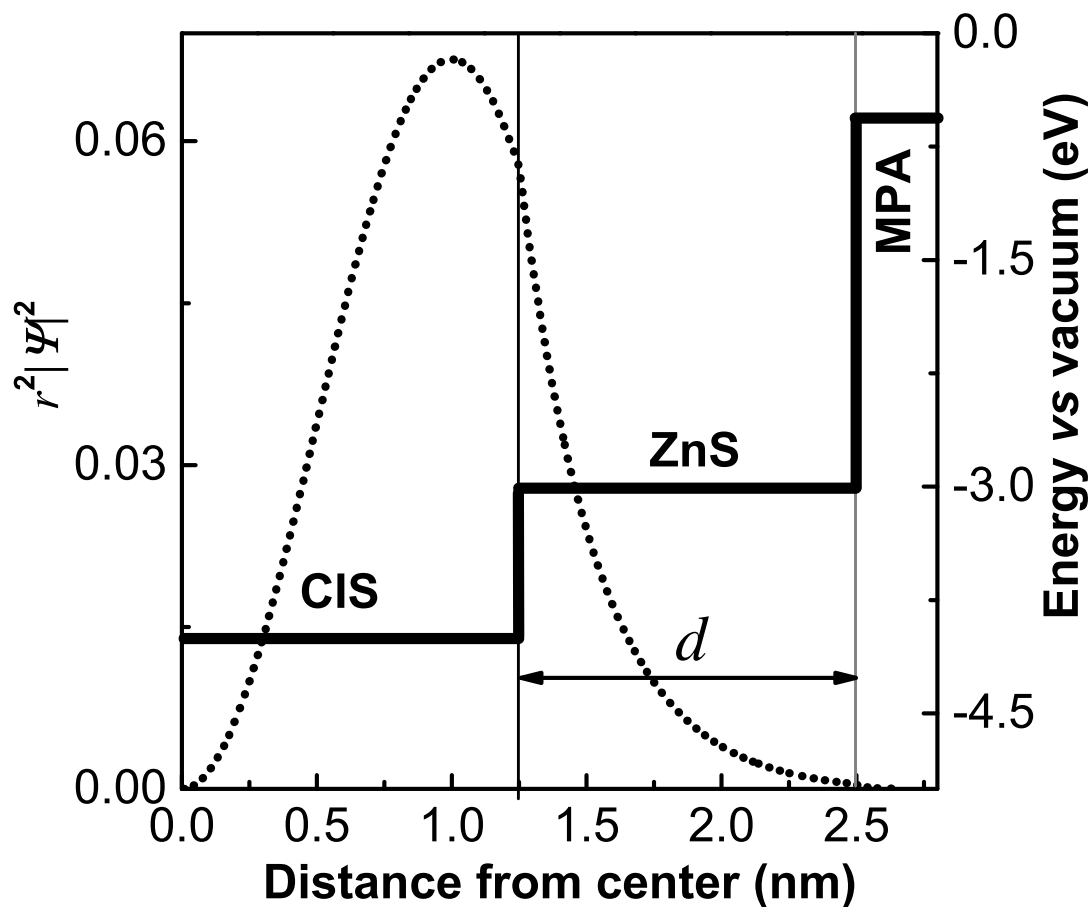
FIG. 4.7 The LUMO level alignment (solid lines) and radial distribution functions (dotted lines) for 1S electron levels of CuInS$_2$/ZnS core/shell QDs (4 ML) with cores 2.5 nm in diameter.

Chapter 5

CuInS$_2$ quantum dot sensitized solar cells

5.1 Introduction

Quantum dot-sensitized solar cells (QDSSCs) have attracted increasing scientific and technical interests and they are considered as an emerging alternative for next generation photovoltaics due to their low cost, easy fabrication and the possibility of boosting the power conversion efficiency beyond the Shockley-Queisser limit of 33%.[1–3] Quantum dots (QDs) offer many advantages, such as tunable bandgap, high absorption coefficient, multiple exciton generation and extraction of hot electrons. Recently, Nozik et al. successfully demonstrated an internal quantum efficiency of more than 130% in the PbSe QDs-based solar cells.[4] The chalcopyrite-type CuInS$_2$ QDs have been proposed because of their less-toxic components. Besides, the band gap of CuInS$_2$ QDs can be tuned not only by controlling their size and stoichiometry but also by introducing other elements such as zinc, hence they are considered to be an ideal material for QDSSCs.[5–12, 16, 17]

At the beginning, CuInS$_2$ QDSSCs showed a power conversion efficiency of less than

1% because of the poor charge separation and the serious electron-hole recombination at the interface between TiO_2 and electrolyte.[13] Recently, the charge recombination at TiO_2/electrolyte interfaces was suppressed by passivizing a CdS buffer layer and the efficiency of $CuInS_2$ QDSSCs were increased to 2.52%.[14–16] Very recently, Teng et al. further improved the $CuInS_2$ QDSSCs by optimizing the CdS passivation layer and they achieved a power conversion efficiency of 4.2%.[17] The trap states at QDs surface play a crucial role in degrading the performance of the QDSSCs. Although the defects at surface of the QDs can be effectively passivated by the CdS or ZnS shells, the actual power conversion efficiency of the QDSSCs is far below the value in dye sensitized solar cells (DSSCs). The origin of such limited performance was attributed to the lowly efficient charge transfer from $CuInS_2$ QDs to external electrodes.

The charge transfer from $CuInS_2$ QDs is the primary event leading to photocurrent generation in QDSSCs. In our previous work,[18] we studied the electron transfer processes from $CuInS_2$ QDs to TiO_2 films and found that the rate and efficiency of electron transfer could be controlled by changing the core diameter. However, the decrease in the size increases both the electron energy and surface densities. It will increase the rate of both the electron transfer and electron trapping at surface defects. Therefore, it remains difficult to optimize the overall charge separation efficiency by selectively and rationally controlling the competing processes in bare QDs.

The recent development in the synthesis of colloidal QDs has led to the preparation of more sophisticated core/shell QDs with multiple component materials and shapes that can be tuned for desired functions. For example, CdX and ZnX (X=S, Se) based semiconductor materials have been extensively tailored and combined into spherical core/shell QDs.[19] In chapter 4, we observed that the rate and efficiency of the electron transfer from $CuInS_2$/ZnS core/shell QDs to TiO_2 films decreased significantly with increasing thickness of ZnS shell. However, it should be noted that the rate and efficiency of elec-

tron transfer can be tuned by controlling the electron densities at QDs surface by means of wave function engineering in core/shell $CuInS_2$ QDs. Compared with type I CIS/ZnS core/shell QDs, the quasi-type II $CuInS_2$/CdS core/shell QDs showed the enhanced delocalization of electron wave function from core to CdS shell due to lower conduction band offset. The CdS shells do not act as barriers but bridges for the electron transfer from $CuInS_2$ QDs. Therefore, the wave function engineering in quasi-type II $CuInS_2$/CdS core/shell QDs offers additional opportunities to effectively control their charge transfer properties, enabling rational design of new types of QDs sensitizers with improved light harvesting and charge separation efficiency in QDSSCs.

In this chapter, a quasi-type II $CuInS_2$/CdS core/shell QDs sensitizer was selected to assemble the QDSSCs and compared with reference $CuInS_2$ bare QDs and type I $CuInS_2$/ZnS core/shell QDs based solar cells. The effect of band alignment and surface states on electron transfer from the $CuInS_2$ QDs to TiO_2 films was studied in detail. More efficient electron transfer was observed from quasi-type II $CuInS_2$/CdS core/shell QDs than that from type I $CuInS_2$/ZnS core/shell QDs to TiO_2 films due to the enhanced delocalization of the electron wave function from the core to the shell. Under AM 1.5G illumination at 100 mW cm^{-2}, the CdS-$CuInS_2$/CdS core/shell QDs co-sensitized solar cell exhibited a power conversion efficiency of 2.27%. The performance was enhanced because of the CdS coating. The CdS coating facilitated the separation of photogenerated electrons and holes in the CdS layers and $CuInS_2$ QDs.

5.2 Experimental

5.2.1 Preparation of the photoelectrodes

The synthesis of $CuInS_2$ QDs, $CuInS_2$/CdS and $CuInS_2$/ZnS core/shell QDs were described in chapter 2. The $CuInS_2$/CdS and $CuInS_2$/ZnS core/shell QDs were synthesized

from the same $CuInS_2$ core QDs 2.5 nm in diameter.

The fluorine doped tin oxide (FTO) substrates were cleaned with soap water soaked in an ultrasonic bath and sonicated in distilled water, acetone and alcohol for 10 minutes for each cleaning step. Pure anatase TiO_2 was employed to construct transparent TiO_2 photoelectrodes. Metallic oxide films of TiO_2 were formed by the doctor blade method. It spread the TiO_2 paste on the FTO glass.[16,17] The thin films were dried at 120 °C for 30 min and then sintered in air at 450 °C for 1 hour. This TiO_2 films were used as the electrode substrate for QDs sensitization. To attach linker molecules to the TiO_2 surface, the TiO_2 films were immersed in an acetonitrile solution of MPA (1 M) and sulfuric acid (0.1 M) for 12 h. This process leads to wrapping the metallic oxide film with thiol ligands. The functionalized metallic oxide film was immersed in QDs solution for 12 h or days to get saturated adsorption of QDs onto the TiO_2 film.

The CdS passivation layer was achieved by means of successive ionic layer adsorption and reaction (SILAR) according to the procedure given in the literature.[16,17] Briefly, the QD modified TiO_2 electrodes were first dipped into an ethanol solution containing $Cd(NO_3)_2$ (0.05M) for 1 min, and then immersed into a Na_2S (0.05 M) water/methanol solution (1 : 1 by volume) for 1 min in sequence. The electrodes were thoroughly rinsed with distilled water to remove the excess precursor after each immersion. This procedure was repeated three times to form a CdS passivation layer on the electrodes.

5.2.2 Preparation of the Cu_2S counter electrodes

The Cu_2S-FTO glass counter electrodes were prepared by a modified method.[20] A 15 nm Cu film was deposited on FTO films by means of magnetron sputtering. Then the Cu films were immersed in HCl solution for 5 min. A droplet of an aqueous polysulfide solution containing 1 M Na_2S and 1 M S was added onto thin treated FTO films causing it to suddenly become black, indicating the formation of Cu_2S.

5.2.3 Assembly of CuInS$_2$ QDSSCs

The photoanodes and the Cu$_2$S counter electrodes were sandwiched together with a scotch tape 50 μ m thick as a spacer and polysulfide electrolyte was injected into the cells. The polysulfide electrolyte contains 2 M Na$_2$S, 2 M S and 0.2 M KCl in the water/methanol solution (3 : 7 by volume). The area of the cells was 0.2 cm^2. Normally, a thinner spacer may help the diffusion of redox species.

5.2.4 Characterization

The absorption spectra were recorded on a UV-vis-NIR scanning spectrophotometer. Time-resolved PL was measured by means of a time-correlated single photon counting (TCSPC) with a visible photomultiplier and a 70 ps pulsed diode laser emitting at 375 nm. Time resolution of the TCSPC system was about 1 ns.

Photocurrent$-$voltage characteristics ($J - V$ curves) of QDSSCs were recorded by a source monitor (ADCMT 6242) under illumination with a solar simulator (SAN-EI ELECTRIC, XES-40S2-CE) at 100 mW cm^{-2}. The intensity of the simulated light was calibrated by a reference Si solar cell. All the measurements were conducted under ambient conditions.

5.3 Experimental results and discussion

5.3.1 Core/shell QDs sensitized solar cells

The band level alignments for TiO$_2$, ZnS, CdS and CuInS$_2$ in bulk material are shown in Fig. 5.1.[21–23] The lowest unoccupied molecular orbital (LUMO) level of the porous anatase TiO$_2$ film is obtained by the cyclic voltammetry method to be -4.2 eV, which is lower than the LUMO level of -4.1 eV for the bulk CuInS$_2$. Therefore, the electron

Table 5.1 The efficiency (η_{ET}) and rate (κ_{ET}) of electron transfer from different QDs to TiO$_2$ films.

Sample	κ_{ET} (10^7s^{-1})	η_{ET} (%)
CIS QDs	6.0	69
CIS/ZnS QDs	0.25	38
CIS/CdS QDs	1.0	91

transfer from the CuInS$_2$ to the porous anatase TiO$_2$ films is allowable. In chapter 4, we demonstrated the electron transfer processes from CuInS$_2$/ZnS core/shell quantum dots (QDs) into porous anatase TiO$_2$ films by time-resolved photoluminescence spectroscopy. The CuInS$_2$/ZnS core/shell QDs exhibited type I carrier localization. The electrons and hole are localized in the CuInS$_2$ core. The electrons in the CuInS$_2$ core tunnel through the ZnS barrier 1 eV high to TiO$_2$. It was found that the ZnS barrier significantly blocked the electron transfer from CuInS$_2$/ZnS core/shell QDs to TiO$_2$. The rates of electron transfer decreased exponentially with increasing ZnS shell thickness, in good agreement with the tunneling barrier character. Based on such a verdict, we can expect that the electron transfer from core/shell QDs to TiO$_2$ accelerates in case of a small conduction band offset between core and shell. Therefore, we choose CdS as the shell materials for CuInS$_2$ core QDs. As shown in Fig. 2.3(a), the CdS overgrowth proceeded together with blue shift of the photoluminescence (PL) initially as is the case for the overgrowth ZnS. However, the PL peaks showed a subsequent red shift. This is different from the case of ZnS. The red-shift is consistent with enhanced delocalization of the electron into the CdS layer, similarly to the report by Klimov group.[5]

Furthermore, the eigen function and energy of the electron in CuInS$_2$ QDs were calculated to illustrate the radial distribution of the wave function for the 1S electron by modeling them as a particle confined in a spherical well of finite depth. As seen in Fig. 5.2, the electron wave functions spread into the shell and their amplitudes decrease expo-

nentially with increasing the shell thickness. It is worth mentioning that the conduction band of bulk $CuInS_2$ is only 0.05 eV lower than that of bulk CdS, making the electron wave function delocalize to the CdS shell easier than the ZnS shell. As illustrated in Fig. 5.2, more than half of the electrons are localized in shell in $CuInS_2$/CdS core/shell QDs. The $CuInS_2$/CdS core/shell QDs exhibit quasi-type II carrier localization. The electrons are mainly localized in the shell and the holes are localized in the core.

In Fig. 5.3, PL decay curves of three kinds of QDs deposited on TiO_2 and ZrO_2 films are shown. The LUMO level of the ZrO_2 film was obtained to be -3.17 eV relative to the vacuum level, which is even higher than the LUMO level of -3.65 eV in $CuInS_2$ core QDs.[18] Therefore, the electron can not transfer from $CuInS_2$ QDs to ZrO_2, and thus the observed PL decay curves in this system can be used as a reference. On ZrO_2 films, the PL lifetimes significantly increased in $CuInS_2$/CdS core/shell QDs compared with $CuInS_2$/ZnS core/shell QDs. This is because the overlapping of the electron and hole wave function reduced in quasi-type II $CuInS_2$/CdS core/shell QDs. In chapter 4, we observed that the electron transfer took place in time scale of sub-100-ns which can compete with the recombination processes including both radiative and nonradaitive processes. Therefore, the electron transfer from QDs to TiO_2 should be more efficient in quasi-type II $CuInS_2$/CdS QDs due to their longer exciton lifetimes.

We assume that the average PL lifetimes of the QDs on TiO_2 and ZrO_2 films are given by $\tau_{QD-TiO_2} = 1/(k_R + k_{NR} + k_{ET})$ and $\tau_{QD-ZrO_2} = 1/(k_R + k_{NR})$, respectively, where k_R and k_{NR} are radiative and nonradiative decay rates for QDs, respectively. The electron transfer rate (k_{ET}) and efficiency (η_{ET}) can be calculated as: $k_{ET} = 1/\tau_{QD-TiO_2} - 1/\tau_{QD-ZrO_2}$ and $\eta_{ET} = 1 - \tau_{QD-TiO_2}/\tau_{QD-ZrO_2}$, respectively. The calculated electron transfer rates and efficiencies are summarized in Table 5.1. Both the rate and the efficiency of the electron transfer from $CuInS_2$/ZnS core/shell QDs decreased significantly compared with that from $CuInS_2$ core QDs. As we discussed in chapter 4, the electron transfer rate is proportional

to the existing probability of electrons at the QD surface which decreased significantly with increasing the ZnS shell thickness. The rate of the electron transfer from $CuInS_2/CdS$ core/shell QDs decreased following the same rule. However, the efficiency increased and reached up to a very high efficiency of 91%. The enhanced electron transfer efficiency was attributed to the slower recombination processes (both radiative and nonradaitive) in quasi-type II $CuInS_2/CdS$ core/shell QDs.

Furthermore, the quasi-type II $CuInS_2/CdS$ core/shell QDs sensitizer was selected to assemble the QDSSCs and compared with reference $CuInS_2$ bare QDs and type I $CuInS_2/ZnS$ core/shell QDs based solar cells. The detail of structure of the QDSSCs is shown in Fig. 5.4. The cells are composed of the QD-sensitized electrode, the polysulfide electrolyte and a Cu_2S counter electrode. The most efficient iodide/triiodide (I^-/I_3^-) redox couple in DSSCs is not compatible because of the easy corrosion of the metal chalcogenides QDs in I^-/I_3^-. A polysulfide redox couple (S^{2-}/S_n^{2-}) is a more suitable electrolyte, compared to the alternatives, in terms of QD stability and redox activity.[17, 24, 25] Moreover, in the polysulfide electrolyte, Cu_2S counter electrodes give lower over-potential.[26]

Figure 5.5 shows the $J-V$ curves of the QDSSCs sensitized with three different kinds of QDs. All the device parameters are summarized in Table 5.2. For the $CuInS_2/ZnS$ core/shell QDs sensitized solar cell, the power conversion efficiency is very low (0.03%), which is ascribed to the low electron transfer efficiency. Otherwise, the ZnS shell also acted as a 1 eV barrier for hole transfer. The high barrier might significantly block the hole transfer from $CuInS_2/ZnS$ core/shell QDs. The efficiencies for the $CuInS_2$ QDs and $CuInS_2/CdS$ core/shell QDs sensitized cells are 0.25% and 0.32%, respectively. Most importantly, the QDSSCs using $CuInS_2/CdS$ core/shell QDs as sensitizers exhibit the better performance with efficiency of 0.32%, slight higher than those of QDSSCs employing $CuInS_2$ QDs and $CuInS_2/ZnS$ core/shell QDs. It is meaningful to note that the CdS shell is beneficial for further improving the performance of $TiO_2/$ $CuInS_2$ QDSSCs with enhanced

Table 5.2 Device characteristics for different kinds of QDs sensitized solar cells.

Sample	V_{OC} (V)	J_{SC} (mA cm^{-2})	FF	η (%)
CIS QDs	0.42	1.42	0.42	0.25
CIS/ZnS QDs	0.26	0.53	0.22	0.03
CIS/CdS QDs	0.43	1.52	0.44	0.29

J_{SC}, which is consistent with the enhanced electron transfer efficiency from CuInS$_2$/CdS core/shell QDs. As discussed above, the CuInS$_2$/CdS core/shell QDs exhibited quasi-type II carrier localization. This unique feature enables the photogenerated electron-hole pairs to efficiently separate from QDs. Therefore, the spatial separation of electrons can be efficiently collected by the external circuit. Another important thing is the extraction of the holes. It appears that the holes are localized in CuInS$_2$, leading to inefficient reaction with the external environment for oxidative reactions, which is detrimental in QDSSCs. However, our work shows that the CuInS$_2$ core confined photoinduced holes can be extracted to the polysulfide electrolyte in QDSSCs. In addition, recent studies had experimentally demonstrated that core-localized holes can be extracted by using hole scavenging surfactants.[27]

5.3.2 Synergistic effect of QDs-CdS co-sensitization

Even for CuInS$_2$/CdS core/shell QDs sensitized solar cells, the power conversion efficiency is very low (0.32%), which is ascribed to the limited light absorption of QDs and serious electron and hole recombination at the interface between TiO$_2$ and polysulfide electrolyte. It is because the TiO$_2$ surface is not covered completely by QDs. A process of SILAR deposition of CdS was conducted to enhance the coverage of the TiO$_2$ surface and to enhance the light absorption by photoelectrodes.[16,17] In addition, surface states and dangling bonds of the QDs can be removed through the passivation by CdS layers.

The absorption spectra of the photoelectrodes coated with CdS by SILAR cycles are

shown in Fig. 5.6. The absorption increases with increasing the SILAR cycles, and becomes saturated after three cycles. The color of the $CuInS_2$/CdS core/shell QDs sensitized photoelectrodes was originally deep red, becoming pale orange or yellowish when it was coated with CdS by three SILAR cycles. Besides, the CdS formed after 3 cycles of SILAR deposition should have a size beyond the quantum confinement region because the absorption edge of the deposited CdS was close to that of bulk CdS (525 nm). Therefore, the delocalization of the electron into the CdS shells from the $CuInS_2$ core was further enhanced by additional CdS passivation.

Figure 5.7 shows the comparison of the J-V characteristics of the QDSSCs assembled with $CuInS_2$/CdS core/shell QDs sensitized photoanodes, before and after the anodes were coated with the CdS passivation layer. The photovoltaic parameters of the QDSSCs assembled photoanodes coated with the CdS passivation layer are summarized in the inset of Fig. 5.7. Under AM 1.5G illumination at 100 mW cm^{-2}, the $CuInS_2$/CdS QDs-CdS co-sensitized solar cell exhibited a short-circuit photocurrent (J_{SC}) of 8.6 mA cm^{-2}, an open-circuit photovoltage (V_{OC}) of 0.46 V, a fill factor of 0.47 and a power conversion efficiency of 1.85%. The J_{SC} increases dramatically by the introduction of the CdS passivation layer, which is consistent with the result reported in the literature.[17] The additional CdS passivation on the photoelectrodes provides high surface coverage to prevent interfacial recombination of the photogenerated charges between TiO_2 films and electrolyte. The role of CdS passivation of the photoelectrodes may be one of the critical mechanisms for enhancing the J_{SC} value in QDSSCs.

As we discussed above, the CdS passivation can effectively suppress the electron leakage to the electrolyte. However, the valence band edge of the CdS layers is higher than that of the $CuInS_2$ QDs, which prohibits the hole transfer from the QDs to electrolyte. To optimize the solar cells further, we deposited the CdS films on the TiO_2 films in advance, and then we sensitized $CuInS_2$/CdS core/shell QDs on the CdS films. As shown in figure

71

5.7, the CdS-CuInS$_2$/CdS core/shell QDs co-sensitized solar cells exhibited a J_{SC} of 9.3 mA cm^{-2}, an V_{OC} of 0.48 V, a fill factor of 0.50 and a power conversion efficiency of 2.27%. The performance is better than the CuInS$_2$/CdS core/shell QDs-CdS co-sensitized solar cells. As seen in the Figure 5.8, CdS acts as the bifunctional layers. The additional CdS passivation on the photoelectrodes not only absorbs more incident photons for the charge separation, but also provides high surface coverage to prevent interfacial recombination of the photogenerated charges between TiO$_2$ films and electrolyte. Although we have already successfully fabricated the good performance QDSSCs, unambiguous understanding of electron injection and charge recombination kinetics from this quasi-type II QDs require further systematic studies.

5.4 Conclusions

In summary, a quasi-type II CuInS$_2$/CdS core/shell QDs sensitized solar cells was fabricated and compared with the CuInS$_2$ bare QDs and the type I CuInS$_2$/ZnS core/shell QDs sensitized solar cells. More efficient electron transfer was observed from quasi-type II CuInS$_2$/CdS core/shell QDs to TiO$_2$ films. The enhanced electron transfer efficiency was attributed to the slower recombination processes (both radiative and nonradiative) in quasi-type II CuInS$_2$/CdS core/shell QDs. Besides, the observed improvement of QDSSCs with CuInS$_2$/CdS core/shell QDs was attributed to have higher efficiency of the electron transfer into TiO$_2$ films. Furthermore, The CdS passivation layers were introduced to absorbs more incident photons and to prevent interfacial recombination, which dramatically improved the performance of the QDSSCs.

Bibliography

[1] A. J. Nozik, Phys. E. **14**, 115 (2002).

[2] R. D. Schaller and V. I. Klimov, Phys. Rev. Lett. **92**, 186601 (2004).

[3] S. Shockley and H. J. Queisser, J. Appl. Phys. **32**, 510 (1961).

[4] O. E. Semonin, J. M. Luther, S. Choi, H. Y. Chen, J. Gao, A. J. Nozik and M. C. Beard, Science **334**, 1530 (2011).

[5] L. Li, A. Pandey, D. J. Werder, B. P. Khanal, J. M. Pietryga, and V. I. Klimov, J. Am. Chem. Soc. **133**, 1176 (2011).

[6] H. Zhong, S. S. Lo, T. Mirkovic, Y. Li, Y. Ding, Y. Li, and G. D. Scholes, ACS Nano. **4**, 5253 (2010).

[7] W. S. Song and H. Yang, Appl. Phys. Lett. **100**, 183104 (2012).

[8] B. Chen, H. Zhong, W. Zhang, Z. Tan, Y. Li, C. Yu, T. Zhai, Y. Bando, S. Yang, and B. Zou, Adv. Funct. Mater. **22**, 2081 (2012).

[9] J. Zhang, R. Xie, and W. Yang, Chem. Mater. **23**, 3357 (2011).

[10] W. Zhang and X. Zhong, Inorg. Chem. **50**, 4065 (2011).

[11] X. Tang, W. Cheng, E. S. G. Choo, and J. Xue, Chem. Commun. **47**, 5217 (2011).

[12] X. Yuan, J. L. Zhao, P. T. Jing, W. J. Zhang, H. B. Li, L. G. Zhang, X. H. Zhong, and Y. Masumoto, J. Phys. Chem. C. **116**, 11973 (2012).

[13] K. T. Kuo, D. M. Liu, S. Y. Chen and C. C. Lin, J. Mater. Chem. **19**, 6780 (2009).

[14] J. Y. Chang, L. F. Su, C. H. Li, C. C. Chang and J. M. Lin, Chem. Commun. **48**, 4848 (2012).

[15] G. P. Xu, S. L. Ji, C. H. Miao, G. D. Liu and C. H. Ye, J. Mater. Chem. **22**, 4890 (2012).

[16] T. L. Li, Y. L. Lee and H. S. Teng, J. Mater. Chem. **21**, 5089 (2011).

[17] T. L. Li, Y. L. Lee and H. S. Teng, Energy Environ. Sci. **5**, 5315 (2012).

[18] J. H. Sun, J. L. Zhao, and Y. Masumoto, Appl. Phys. Lett. **102**, 053119 (2013).

[19] P. Reiss, M. Protiere, L. Li, Small **5**, 154 (2009).

[20] V. Gonzalez-Pedro, X. Xu, I. Mora-Sero, J. Bisquert, ACS Nano. **4**, 5783 (2010).

[21] H. Zhu, N. Song, and T. Lian, J. Am. Chem. Soc. **132**, 15038 (2010).

[22] P. K. Santra, P. V. Nair, K. G. Thomas, P. V. Kamat, J. Phys. Chem. Lett. **4**, 722 (2013).

[23] E. Arici, N. S. Sariciftci, D. Meissner, Adv. Funct. Mater. **13**, 165 (2003).

[24] H. Lee, M. K. Wang, P. Chen, D. R. Gamelin, S. M. Zakeeruddin, M. Grätzel and M. K. Nazeeruddin, Nano Lett. **9**, 4221 (2009).

[25] P. Yu, K. Zhu, A. G. Norman, S. Ferrere, A. J. Frank and A. J. Nozik, J. Phys. Chem. B. **110**, 25451 (2006).

[26] Z. Yang, C.-Y. Chen, C.-W. Liu, C.-L. Li and H.-T. Chang, Adv. Energy Mater. **1**, 259 (2011).

[27] Z. J. Ning, C. Z. Yuan, H. N. Tian, Y. Fu, L. Li, L. C. Sun and H. Agren, J. Mater. Chem. **22**, 6032 (2012).
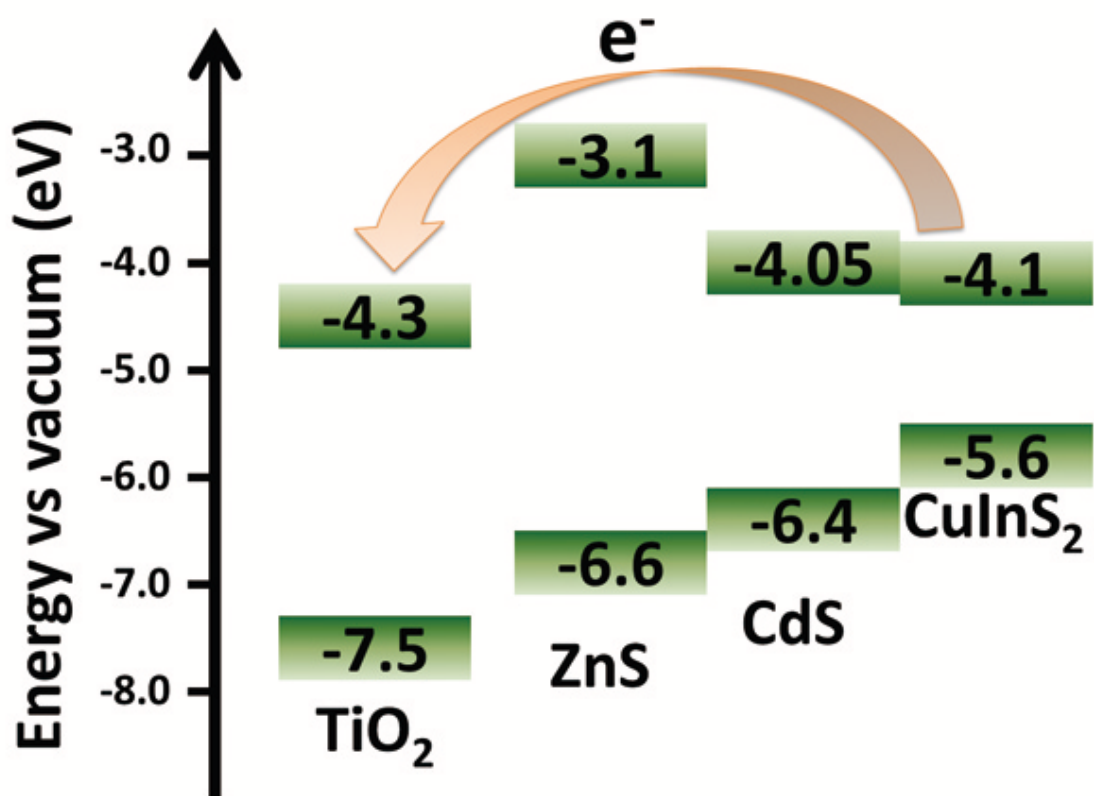
FIG. 5.1 Schematic energy level diagram of bulk TiO_2, ZnS, CdS and $CuInS_2$. All the energy levels are relative to the vacuum level.[21–23]
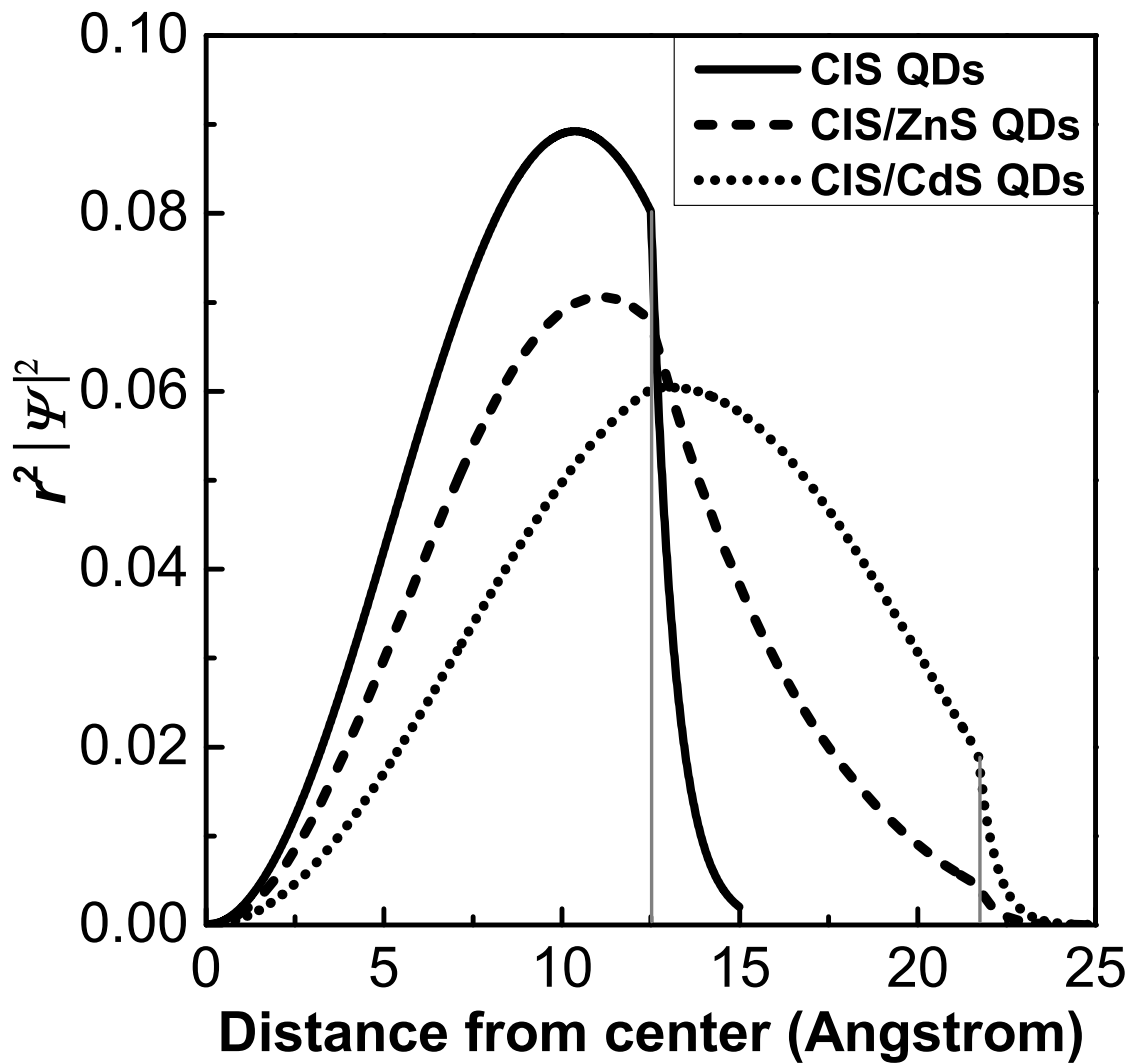
FIG. 5.2 The radial distribution functions of the electrons in 2.5 nm $CuInS_2$ QDs (solid line) $CuInS_2/CdS$ (dotted line) and $CuInS_2/ZnS$ (dashed line) core/shell QDs with the core 2.5 nm in diameter and the shell 0.95 nm thick.
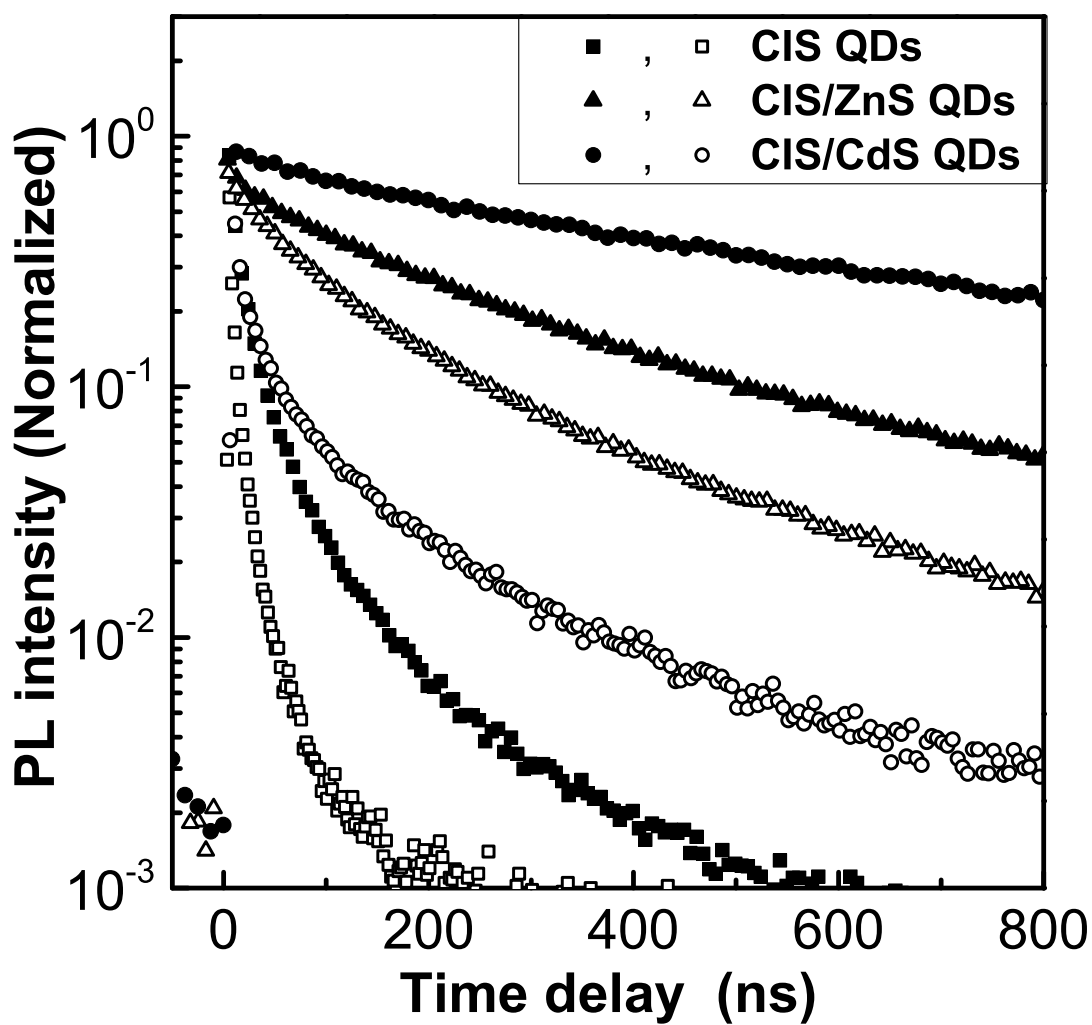
FIG. 5.3 Photoluminescence decay curves of CuInS$_2$ core QDs, CuInS$_2$/ZnS core/shell QDs and CuInS$_2$/CdS core/shell QDs deposited on the ZrO$_2$ (solid masks) and TiO$_2$ films (open masks).
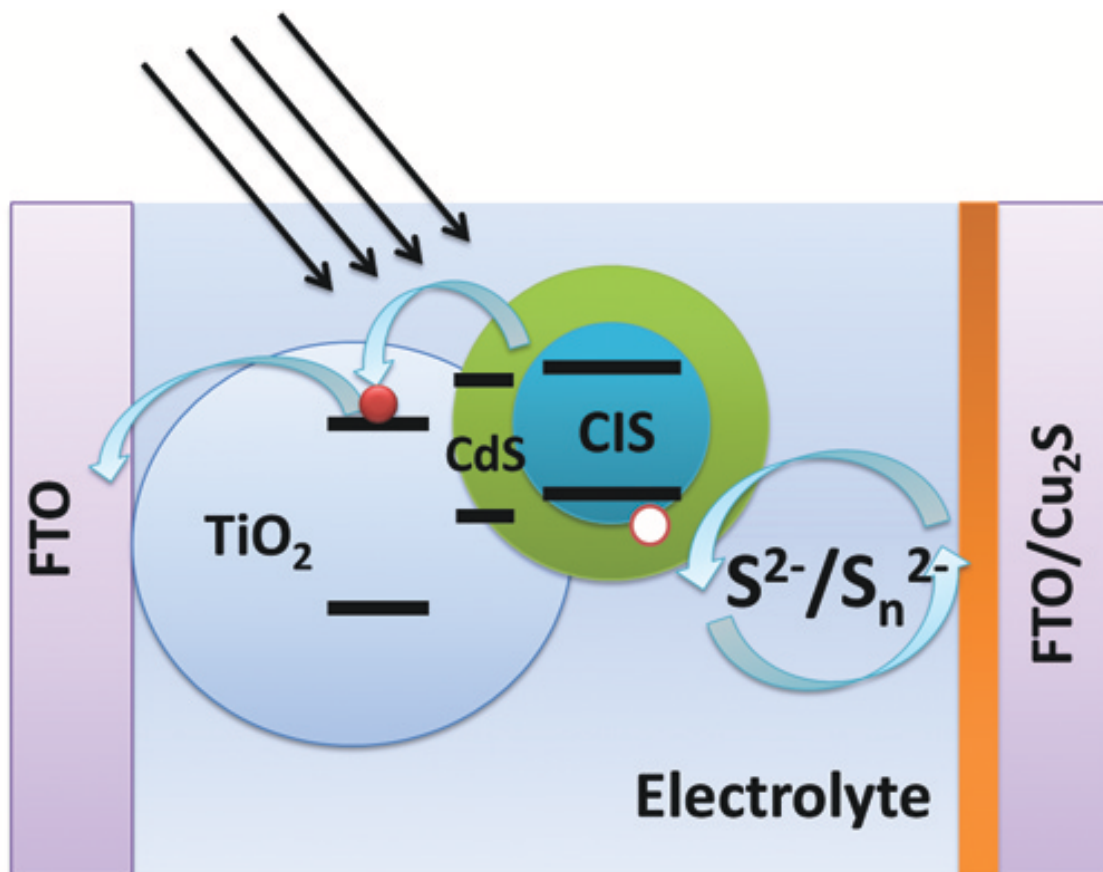
FIG. 5.4 Electronic processes and the structure of the CuInS$_2$/CdS core/shell QDs sensitized solar cells.
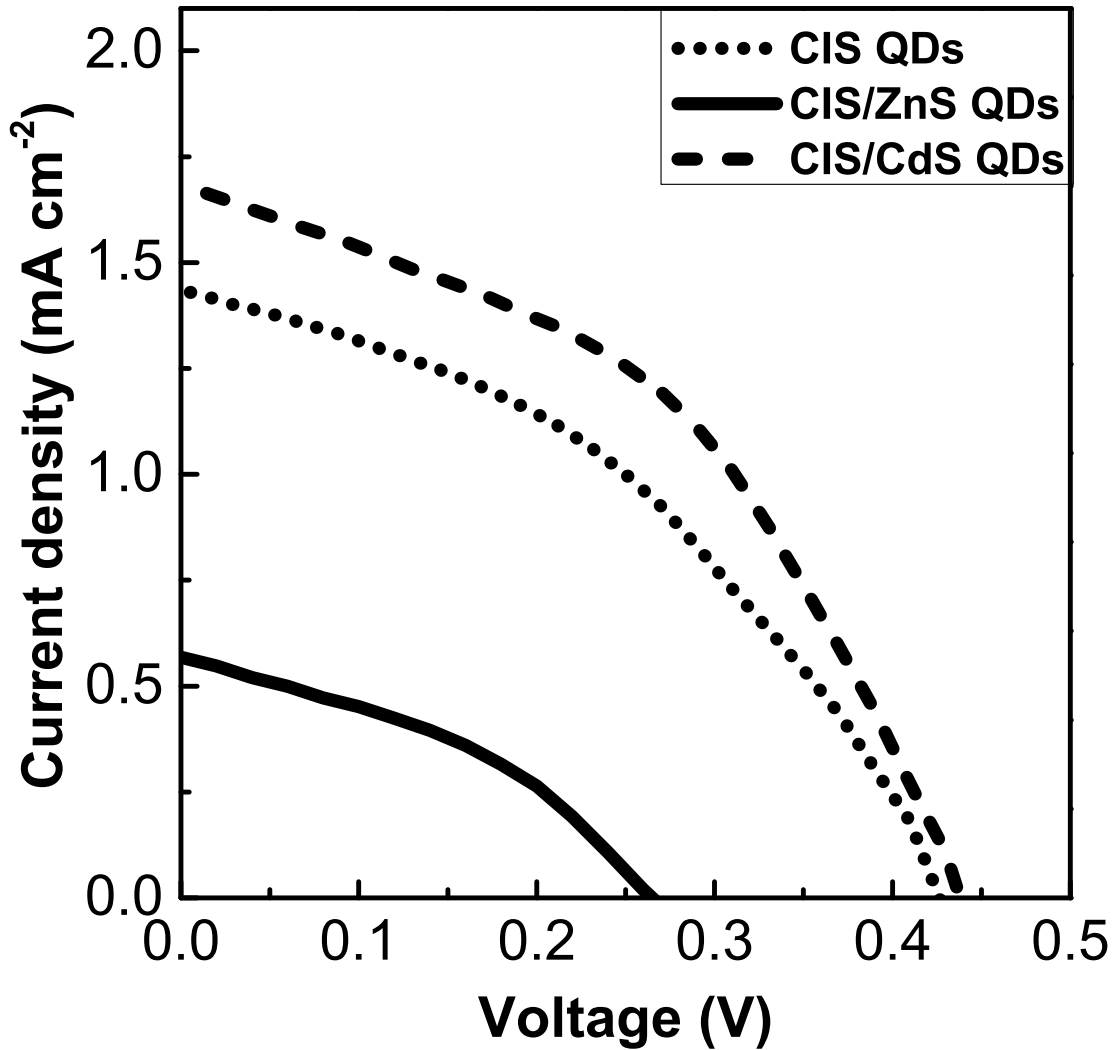
FIG. 5.5 Photocurrent-voltage characteristics of QDs sensitized solar cells assembled with $CuInS_2$ core QDs, $CuInS_2/ZnS$ core/shell QDs and $CuInS_2/CdS$ core/shell QDs photoanode and the Cu_2S counter electrodes under AM 1.5G illumination at 100 mW cm^{-2}.
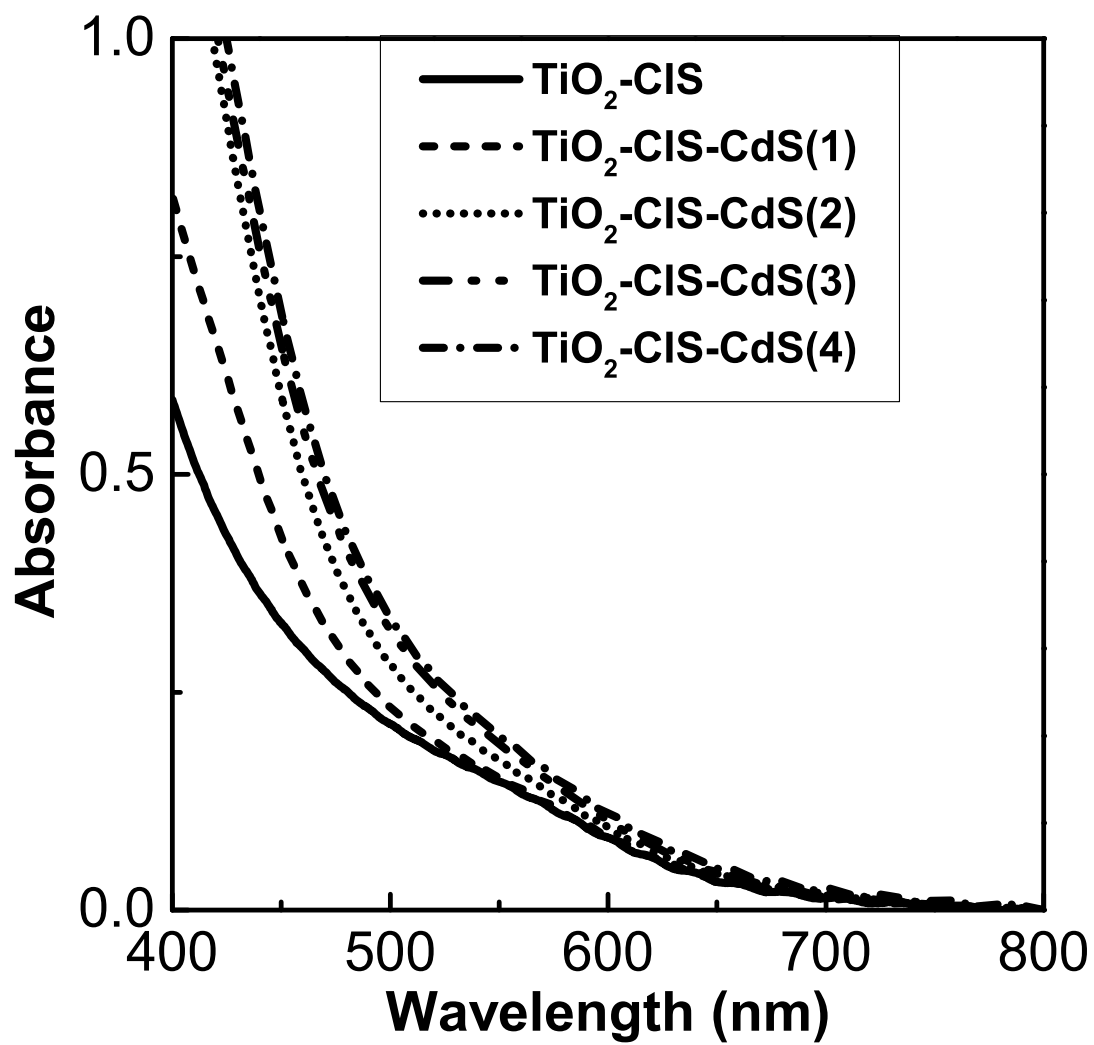
FIG. 5.6 Optical absorption spectra of TiO_2 films sensitized with 2.5 nm $CuInS_2$ QDs. The number in parentheses represent the cycle number of successive ionic layer adsorption and reaction (SILAR) coating.
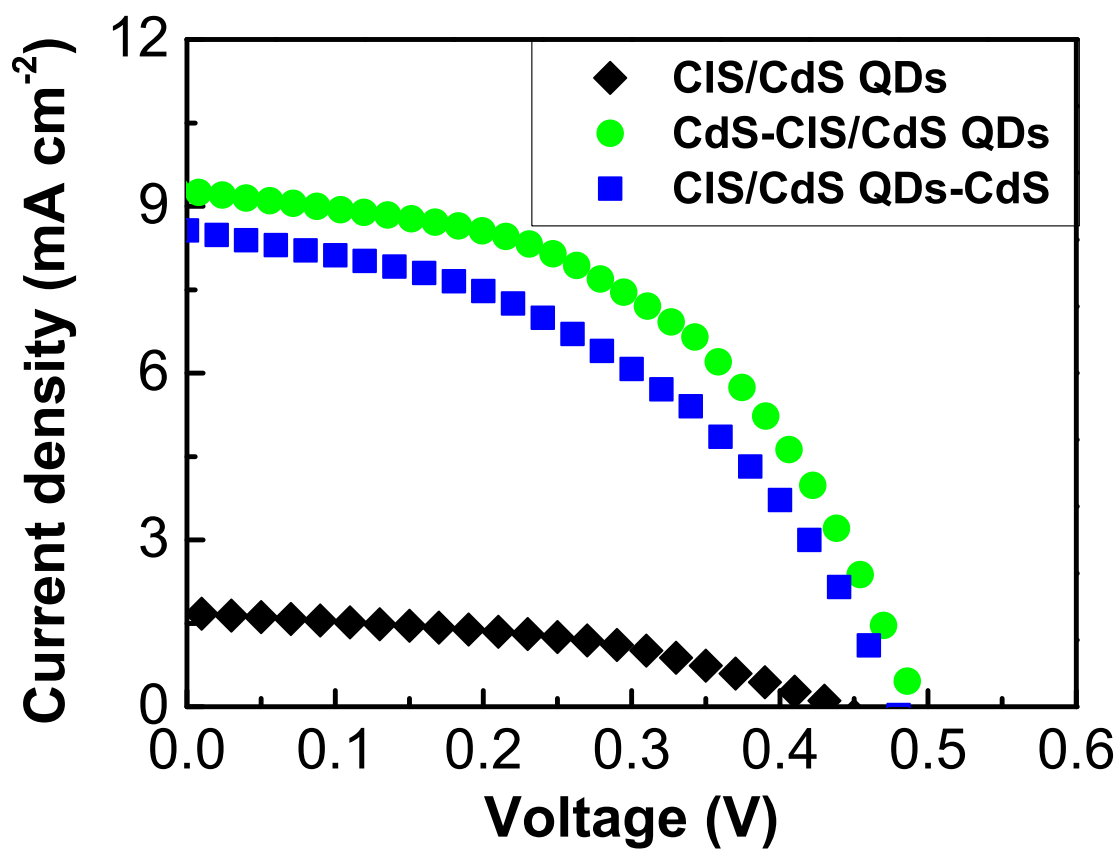
FIG. 5.7 Photocurrent-voltage characteristics of the $CuInS_2/CdS$ core/shell QD-s sensitized solar cells, CdS-$CuInS_2/CdS$ core/shell QDs co-sensitized solar cells and $CuInS_2/CdS$ core/shell QDs-CdS co-sensitized solar cells.
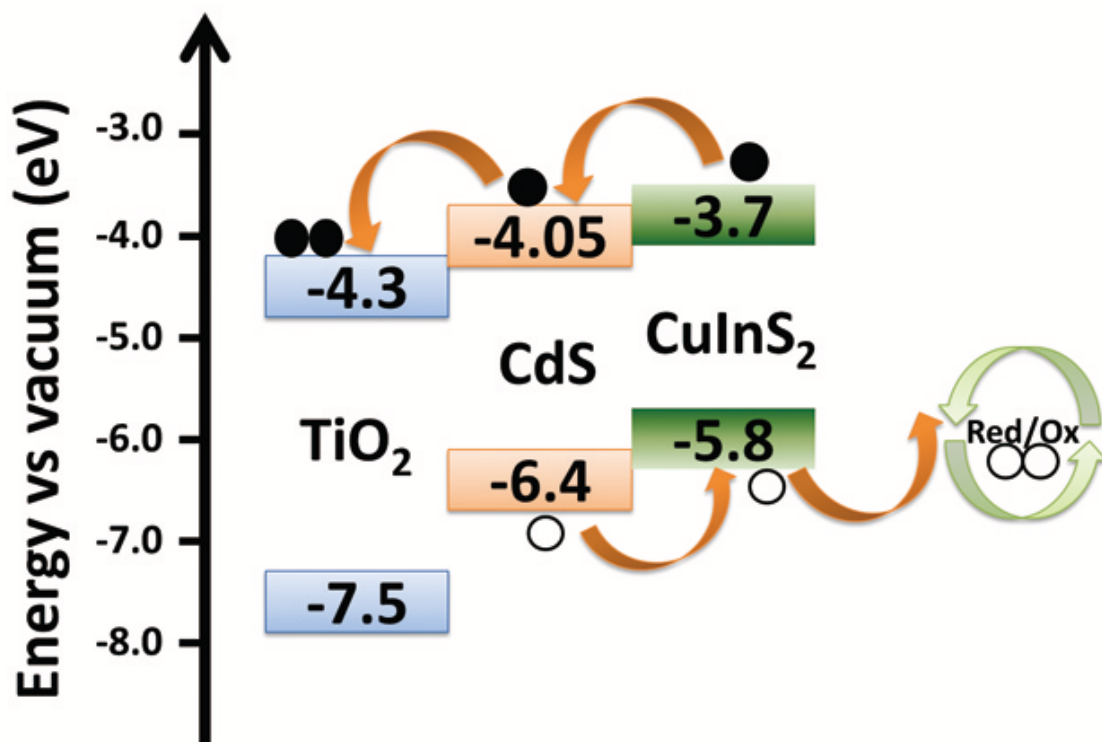
FIG. 5.8 Schematic diagram showing the charge separation processes of TiO_2 films co-sensitized with CdS layers and $CuInS_2$/CdS core/shell QDs.

Chapter 6

Conclusions

In this thesis, we studied the intrinsic characters of the exciton states in CuInS$_2$ QDs and investigated the way to transfer the 1S electrons to TiO$_2$ for improving the performance of the CuInS$_2$ QDs sensitized solar cells.

The mechanism for optical nonlinearities and ultrafast carrier dynamics in CuInS$_2$ QDs were investigated by means of femtosecond transient absorption (TA) spectroscopy. We demonstrated that the TA bleaching comes from filling of electron quantized levels, allowing us to know the dynamics of the 1S electron in CuInS$_2$ QDs. The sub-100-ps electron trapping at surface defects in bare CuInS$_2$ QDs accelerates with decreasing the QD size scaling with the inverse of QD radius ($1/\tau_i \propto R^{-1.8}$). These surface trapping states were effectively passivated in CuInS$_2$/ZnS core/shell QDs. Therefore, the long-lifetime emission in CuInS$_2$ QDs is most entirely involved with the transition from a 1S electron state to a hole-localized state. The results clearly show the intrinsic characters of the 1S electron states in CuInS$_2$ QDs.

We systematically investigated the 1S electron transfer from the CuInS$_2$ QDs and CuInS$_2$/ZnS core/shell QDs to the TiO$_2$ film by means of time-resolved photoluminescence spectroscopy. We observed that the electron transfer took place in time scale of sub-100-ns which can compete with the recombination processes. The electron transfer

rate as a function of shell thickness was well expressed by an exponential function for the core/shell QDs with core diameters of 2.5 nm and 4.0 nm. This trend is well explained by the electron tunneling calculation of the core/shell QDs. The electron transfer rate is proportional to the existing probability of electrons at the QD surface decreasing exponentially with increasing the shell thickness. The results show the way to control the rate and efficiency of electron transfer by tuning the electron densities at QDs surface via electron wave function engineering in core/shell $CuInS_2$ QDs.

The effect of band alignment on electron transfer from the core/shell $CuInS_2$ QDs to TiO_2 films was studied. More efficient electron transfer was observed from quasi-type II $CuInS_2$/CdS core/shell QDs than from type I $CuInS_2$/ZnS core/shell QDs to TiO_2 films due to the enhanced delocalization of the electron wave function from the core to the CdS shell. Under AM 1.5G illumination at 100 mW cm^{-2}, the CdS-$CuInS_2$/CdS core/shell QDs co-sensitized solar cell exhibited a short-circuit photocurrent (J_{SC}) of 9.3 mA cm^{-2}, an open-circuit photovoltage (V_{OC}) of 0.48 V, a fill factor of 0.50 and a power conversion efficiency of 2.27%. The improved performance of QDSSCs with $CuInS_2$/CdS core/shell QDs was attributed to higher efficiency of the electron injection from quasi-type II $CuInS_2$/CdS core/shell QDs to TiO_2 films.

Acknowledgements

List of publications

1. **"Ultrafast carrier dynamics in CuInS$_2$ quantum dots"**,

   Jianhui Sun, Dehua Zhu, Jialong Zhao, Michio Ikezawa, Xiuying Wang, and Yasuaki Masumoto,

   Appl. Phys. Lett. **104**, 023118 (2014).

2. **"Shell-thickness-dependent photoinduced electron transfer from CuInS$_2$/ZnS quantum dots to TiO$_2$ films"**,

   Jianhui Sun, Jialong Zhao, and Yasuaki Masumoto,

   Appl. Phys. Lett. **102**, 053119 (2013).